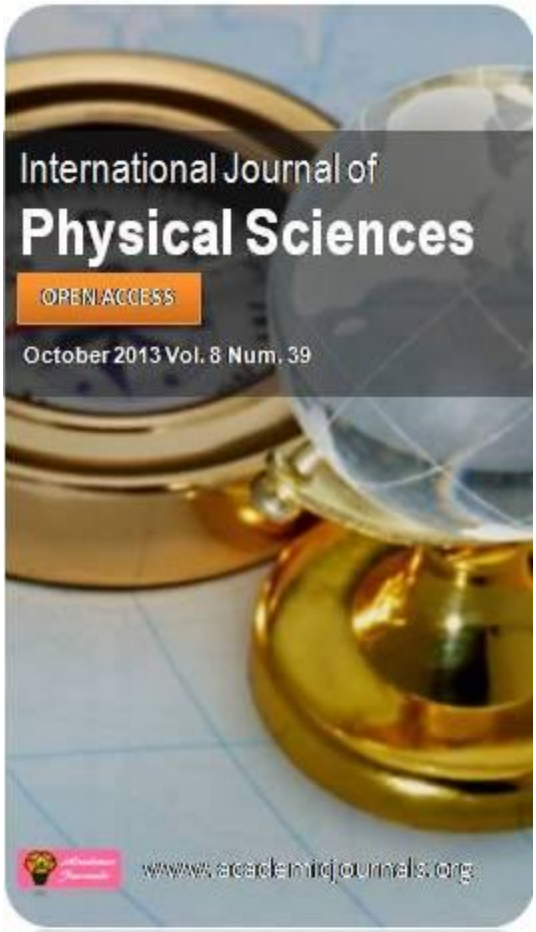

International Journal of Physical Sciences

October 2013 - Vol. 8 Num. 39

Submit manuscripts: www.ms.academicjournals.org

Editorial Office: ijps@academicjournals.org

URL: www.academicjournals.org

academicJournals

ABOUT IJPS

The **International Journal of Physical Sciences (IJPS)** is published weekly (one volume per year) by Academic Journals.

International Journal of Physical Sciences (IJPS) is an open access journal that publishes high-quality solicited and unsolicited articles, in English, in all Physics and chemistry including artificial intelligence, neural processing, nuclear and particle physics, geophysics, physics in medicine and biology, plasma physics, semiconductor science and technology, wireless and optical communications, materials science, energy and fuels, environmental science and technology, combinatorial chemistry, natural products, molecular therapeutics, geochemistry, cement and concrete research, metallurgy, crystallography and computer-aided materials design. All articles published in IJPS are peer-reviewed.

Submission of Manuscript

Submit manuscripts as e-mail attachment to the Editorial Office at: ijps@academicjournals.org. A manuscript number will be mailed to the corresponding author shortly after submission.

For all other correspondence that cannot be sent by e-mail, please contact the editorial office (at ijps@academicjournals.org).

The International Journal of Physical Sciences will only accept manuscripts submitted as e-mail attachments.

Please read the **Instructions for Authors** before submitting your manuscript. The manuscript files should be given the last name of the first author.

Editors

Editorial Board

Instructions for Author

Electronic submission of manuscripts is strongly encouraged, provided that the text, tables, and figures are included in a single Microsoft Word file (preferably in Arial font).

The **cover letter** should include the corresponding author's full address and telephone/fax numbers and should be in an e-mail message sent to the Editor, with the file, whose name should begin with the first author's surname, as an attachment.

Article Types

Three types of manuscripts may be submitted:

Regular articles: These should describe new and carefully confirmed findings, and experimental procedures should be given in sufficient detail for others to verify the work. The length of a full paper should be the minimum required to describe and interpret the work clearly.

Short Communications: A Short Communication is suitable for recording the results of complete small investigations or giving details of new models or hypotheses, innovative methods, techniques or apparatus. The style of main sections need not conform to that of full-length papers. Short communications are 2 to 4 printed pages (about 6 to 12 manuscript pages) in length.

Reviews: Submissions of reviews and perspectives covering topics of current interest are welcome and encouraged. Reviews should be concise and no longer than 4-6 printed pages (about 12 to 18 manuscript pages). Reviews are also peer-reviewed.

Review Process

All manuscripts are reviewed by an editor and members of the Editorial Board or qualified outside reviewers. Authors cannot nominate reviewers. Only reviewers randomly selected from our database with specialization in the subject area will be contacted to evaluate the manuscripts. The process will be blind review.

Decisions will be made as rapidly as possible, and the journal strives to return reviewers' comments to authors as fast as possible. The editorial board will re-review manuscripts that are accepted pending revision. It is the goal of the IJPS to publish manuscripts within weeks after submission.

Regular articles

All portions of the manuscript must be typed double-spaced and all pages numbered starting from the title page.

The Title should be a brief phrase describing the contents of the paper. The Title Page should include the authors' full names and affiliations, the name of the corresponding author along with phone, fax and E-mail information. Present addresses of authors should appear as a footnote.

The Abstract should be informative and completely self-explanatory, briefly present the topic, state the scope of the experiments, indicate significant data, and point out major findings and conclusions. The Abstract should be 100 to 200 words in length.. Complete sentences, active verbs, and the third person should be used, and the abstract should be written in the past tense. Standard nomenclature should be used and abbreviations should be avoided. No literature should be cited.

Following the abstract, about 3 to 10 key words that will provide indexing references should be listed.

A list of non-standard **Abbreviations** should be added. In general, non-standard abbreviations should be used only when the full term is very long and used often. Each abbreviation should be spelled out and introduced in parentheses the first time it is used in the text. Only recommended SI units should be used. Authors should use the solidus presentation (mg/ml). Standard abbreviations (such as ATP and DNA) need not be defined.

The Introduction should provide a clear statement of the problem, the relevant literature on the subject, and the proposed approach or solution. It should be understandable to colleagues from a broad range of scientific disciplines.

Materials and methods should be complete enough to allow experiments to be reproduced. However, only truly new procedures should be described in detail; previously published procedures should be cited, and important modifications of published procedures should be mentioned briefly. Capitalize trade names and include the manufacturer's name and address. Subheadings should be used. Methods in general use need not be described in detail.

Results should be presented with clarity and precision. The results should be written in the past tense when describing findings in the authors' experiments. Previously published findings should be written in the present tense. Results should be explained, but largely without referring to the literature. Discussion, speculation and detailed interpretation of data should not be included in the Results but should be put into the Discussion section.

The Discussion should interpret the findings in view of the results obtained in this and in past studies on this topic. State the conclusions in a few sentences at the end of the paper. The Results and Discussion sections can include subheadings, and when appropriate, both sections can be combined.

The Acknowledgments of people, grants, funds, etc should be brief.

Tables should be kept to a minimum and be designed to be as simple as possible. Tables are to be typed double-spaced throughout, including headings and footnotes. Each table should be on a separate page, numbered consecutively in Arabic numerals and supplied with a heading and a legend. Tables should be self-explanatory without reference to the text. The details of the methods used in the experiments should preferably be described in the legend instead of in the text. The same data should not be presented in both table and graph form or repeated in the text.

Figure legends should be typed in numerical order on a separate sheet. Graphics should be prepared using applications capable of generating high resolution GIF, TIFF, JPEG or Powerpoint before pasting in the Microsoft Word manuscript file. Tables should be prepared in Microsoft Word. Use Arabic numerals to designate figures and upper case letters for their parts (Figure 1). Begin each legend with a title and include sufficient description so that the figure is understandable without reading the text of the manuscript. Information given in legends should not be repeated in the text.

References: In the text, a reference identified by means of an author's name should be followed by the date of the reference in parentheses. When there are more than two authors, only the first author's name should be mentioned, followed by 'et al'. In the event that an author cited has had two or more works published during the same year, the reference, both in the text and in the reference list, should be identified by a lower case letter like 'a' and 'b' after the date to distinguish the works.

Examples:

Abayomi (2000), Agindotan et al. (2003), (Kelebeni, 1983), (Usman and Smith, 1992), (Chege, 1998; 1987a,b; Tijani, 1993,1995), (Kumasi et al., 2001)

References should be listed at the end of the paper in alphabetical order. Articles in preparation or articles submitted for publication, unpublished observations, personal communications, etc. should not be included in the reference list but should only be mentioned in the article text (e.g., A. Kingori, University of Nairobi, Kenya, personal communication). Journal names are abbreviated according to Chemical Abstracts. Authors are fully responsible for the accuracy of the references.

Examples:

Ogunseitan OA (1998). Protein method for investigating mercuric reductase gene expression in aquatic environments. Appl. Environ. Microbiol. 64:695-702.

Gueye M, Ndoye I, Dianda M, Danso SKA, Dreyfus B (1997). Active N2 fixation in several Faidherbia albida provenances. Ar. Soil Res. Rehabil. 11:63-70.

Charnley AK (1992). Mechanisms of fungal pathogenesis in insects with particular reference to locusts. In: Lomer CJ, Prior C (eds) Biological Controls of Locusts and Grasshoppers: Proceedings of an international workshop held at Cotonou, Benin. Oxford: CAB International, pp 181-190.

Mundree SG, Farrant JM (2000). Some physiological and molecular insights into the mechanisms of desiccation tolerance in the resurrection plant Xerophyta viscasa Baker. In Cherry et al. (eds) Plant tolerance to abiotic stresses in Agriculture: Role of Genetic Engineering, Kluwer Academic Publishers, Netherlands, pp 201-222.

Short Communications

Short Communications are limited to a maximum of two figures and one table. They should present a complete study that is more limited in scope than is found in full-length papers. The items of manuscript preparation listed above apply to Short Communications with the following differences: (1) Abstracts are limited to 100 words; (2) instead of a separate Materials and Methods section, experimental procedures may be incorporated into Figure Legends and Table footnotes; (3) Results and Discussion should be combined into a single section.

Proofs and Reprints: Electronic proofs will be sent (e-mail attachment) to the corresponding author as a PDF file. Page proofs are considered to be the final version of the manuscript. With the exception of typographical or minor clerical errors, no changes will be made in the manuscript at the proof stage.

International Journal of Physical Sciences

Table of Contents: Volume 8 Number 39, 23 October, 2013

ARTICLES

academicJournals

Vol. 8(39), pp. 1892-1897, 23 October, 2013
DOI: 10.5897/IJPS2013.4052
ISSN 1992 - 1950 © 2013 Academic Journals
http://www.academicjournals.org/IJPS

International Journal of Physical Sciences

Full Length Research Paper

Studies on the mechanical properties of glycine lithium chloride NLO single crystal

Suresh Sagadevan[1]* and R. Varatharajan[2]

[1]Department of Physics, Sree Sastha Institute of Engineering and Technology, Chembarambakkam, Chennai-600 123, India.
[2]Department of Mechanical Engineering, Sree Sastha Institute of Engineering and Technology, Chembarambakkam, Chennai-600 123, India.

Accepted 22 October, 2013

The microhardness study reveals the mechanical strength of the grown crystal. The Vicker's and Knoop hardness studies were performed to understand the mechanical behavior of the glycine lithium chloride crystals. The Vicker's and Knoop microhardness numbers (H_V and H_K) for the crystal were found for different loads. It is found that these numbers increase with an increase in the load. The Mayer's index *(n)* was found to be greater than 1.6 predicting a soft-material nature. The fracture toughness value (K_c), was determined from the measurements of the crack length. The brittleness indices (B_i) were found for the grown crystals. Using Wooster's empirical relation, the elastic stiffness constant (C_{11}) was calculated from the Vicker's hardness values at different loads. The Young's modulus was also calculated from Knoop microhardness values.

Key words: Microhardness number, Mayer's index, fracture toughness, brittleness indices, elastic stiffness coefficient, Young's modulus.

INTRODUCTION

Hardness is an important factor in the choice of ceramics for abrasives, bearings, tool bits, wear resistance coatings etc. Hardness is a measure of resistance against lattice destruction or the resistance offered to permanent deformation or damage. Measurement of hardness is a destructive testing method to determine the mechanical behaviour of the materials. As pointed out by Shaw (1973), the term hardness is having different meanings to different people depending upon their areas of interest. For example, it is the resistance to penetration to a metallurgist, the resistance to cutting to a machinist, the resistance to wear and tear to a lubrication engineer and a measure of flow of stress to a design engineer. All these actions are related to the plastic stress of the material. For hard and brittle materials, the hardness test has proved to be a valuable technique in the general study of plastic deformation (Westbrook and Conrad, 1971). The hardness depends not only on the properties of the materials under test but also largely on the conditions of measurement. Microhardness tests have been applied to fine components of clock and instrument mechanisms, thin metal strip, foils, wires, metallic fibers, thin galvanic coatings, artificial oxide films, etc., as well as the thin surface layers of metals which change their properties as a result of mechanical treatments such as machining, rolling, friction and other effects. The microhardness method is widely used for studying the individual structural constituent elements of metallic alloys, minerals, glasses, enamels and artificial abrasives.

The mechanical strength of a material plays a key role in device fabrication. It is a measure of the resistance the lattice offers to local deformation (Mott, 1958).

*Corresponding author. E-mail-sureshsagadevan@yahoo.co.in

Hardness is one of the important mechanical properties of the materials (Xingtao et al., 2008; Ke and Dong, 2009; Ke and Dong, 2010). It can be used as a suitable measure of the plastic properties and strength of a material (Desai and Rai, 1983). Stillwel (1938) defined hardness as resistance against lattice destruction, whereas Ashby (1951) defined it as the ability of a crystal to resist a structural breakdown under applied stress. This resistance is an intrinsic property of the crystal. The hardness properties are related to the crystal structure of the material and microhardness tests have been carried out to understand the plasticity of the crystals. Also, the hardness of the crystal is dependent on the type of chemical bonding, which may differ along the crystallographic directions. Hardness is generally taken as a ratio of the applied load to the area of indentation. The measurement of hardness is very important, as far as the fabrication of devices is concerned.

In the present investigation, attention is focused on the mechanical properties of glycine lithium chloride single crystals such as Meyer's index number, brittle index and fracture toughness calculated from Vicker's microhardness number (H_V). The Young's modulus was calculated from the Knoop hardness test.

MATERIALS AND METHODS

Experimental procedure

Glycine lithium chloride single crystals were synthesized by dissolving glycine and lithium chloride in the molar ratio of 1:1 in distilled water. The solution was stirred continuously using a magnetic stirrer. The prepared solution was filtered and kept undisturbed at room temperature. The beaker was closed with a porously sealed cover and the solution in the beaker was allowed to evaporate. A few days later, tiny crystals were seen in the beaker. Among them, a defect free seed crystal was suspended in the mother solution, which was allowed to evaporate at room temperature. Large size single crystals were obtained due to collection of monomers at the seed crystal sites from the mother solution. The mechanical characterization of glycine lithium chloride crystals were made by Vickers microhardness and Knoop microhardness test. The grown crystal with flat and smooth faces and free from any defects was chosen for the static indentation tests. The surface was polished gently with methanol and mounted properly on the base of the microscope. Now the selected face was indented gently by varying the loads for a dwell period of 10 s using Vickers and Knoop indenter attached to an incident ray research microscope (Mututoyo MH112, Japan).

Vicker's test

Vicker's test is said to be a more reliable method of hardness measurement. In order to get a similar geometrical impression under varying loads, Smith and Sandland (1923) have suggested that a pyramid be substituted for a ball. The Vickers hardness test method consists of indenting the test material with a diamond indenter, in the form of a right pyramid with a square base and an angle of 136° between opposite faces and subjected to a load of 1 to 100 kg (Figure 1). The base of the Vickers pyramid is a square and the depth of indentation corresponds to 1/7th of the indentation diagonal. The longitudinal and transverse diagonals will be in the ratio of 7:1. The full load was normally applied for 10 to 15 s. The two diagonals of the indentation left in the surface of the material after the removal of the load were measured using a microscope, and their average was calculated. The area of the sloping surface of the indentation was calculated.

The Vicker's hardness is the quotient obtained by dividing the kg load by the square mm area of indentation.

$$H_V = \frac{2p\sin\frac{136}{2}}{d^2}$$

$$H_V = 1.8544P/d^2$$

where H_V = Vickers hardness number, P = load in kg, d = arithmetic mean of the two diagonals.

When the mean diagonal of the indentation has been determined, the Vicker's hardness number can be calculated from the above formula. Several different loading settings give practically identical hardness numbers on uniform material, which is much better than the arbitrary changing of scale with the other hardness testing methods. The advantages of the Vicker's hardness test are that extremely accurate readings can be taken, and just one type of indenter is used for all types of metals and surface treatments.

Knoop hardness test

Knoop hardness can be treated as an alternative to the Vickers test, particularly for very thin layers, Fredrick Knoop developed a low-load test with a rhombohedral-shaped diamond indenter. The long diagonal is seven times (7.114 actually) as long as the short diagonal. With this indenter shape, elastic recovery can be held to a minimum. Knoop tests are mainly done at test forces of 10 to 1000 g (Figure 2); so, a high powered microscope is necessary to measure the indent size. Because of this, Knoop tests have mainly been known as microhardness tests. The magnifications required to measure Knoop indents dictate a highly polished test surface. To achieve this surface, the samples are normally mounted and metallurgically polished; therefore Knoop is almost always a destructive test.

The mechanical characterization of the glycine lithium chloride crystals was analyzed by the Vicker's and Knoop microhardness tests. Crystals with flat and smooth faces were chosen for the static indentation tests and the same crystal was mounted on the base of the microscope. The indentations were made gently by varying the loads from 10 to 100 g for a dwell period of 10 s using both the Vicker's diamond pyramid indenter and the Knoop indenter attached to an incident ray research microscope (Mitutoyo MH112, Japan). The intended impression of Vicker's was approximately square in shape. The shape of the impression is dependent on the structure, face and materials used. After unloading, the length of the two diagonals was measured by a calibrated micrometer attached to the eyepiece of the microscope. For each load, at least five well-defined indentations were considered and the average was taken as d. The Vicker's hardness was calculated using the standard formula

$$H_V = 1.8544P/d^2 \quad (1)$$

where P is the applied load in Kg, d in µm and H_V in Kg/mm^2. The Knoop indented impressions were approximately rhombohedral in shape. The average diagonal length (d) was considered for the calculation of the Knoop hardness number (H_K) using the relation

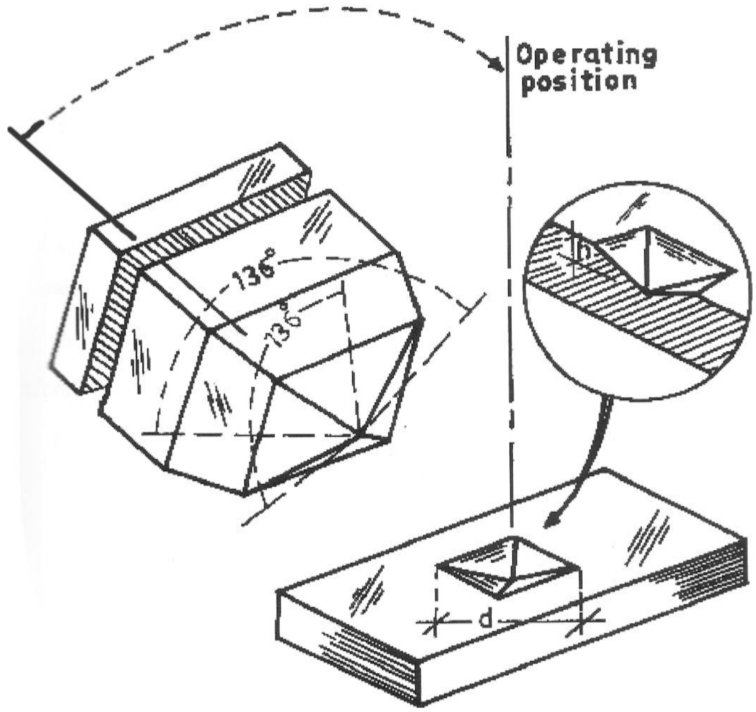

Figure 1. Vickers hardness test.

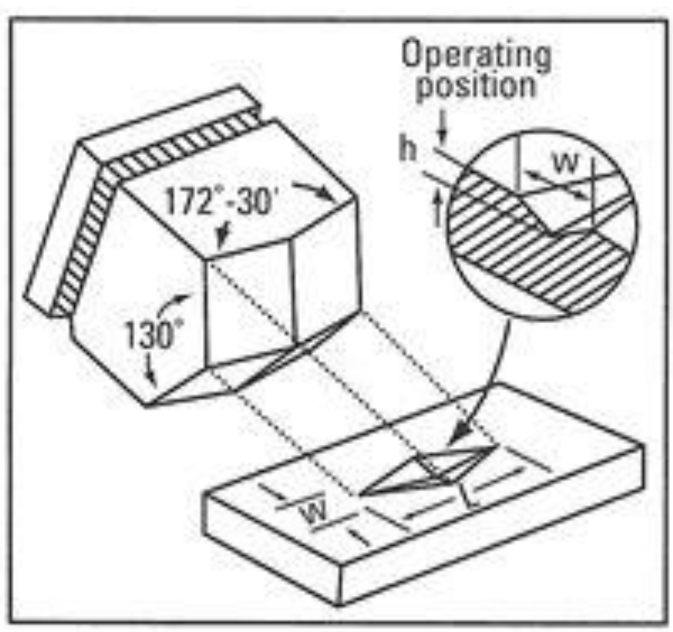

Figure 2. Knoop hardness test.

$$H_K = 14.229\,P/d^2 \quad (2)$$

where P is the applied load in Kg, d in µm and H_K is in kg/mm^2. Beyond 100 g of the applied load, crack initiation and fragmentation were observed. So the hardness test could not be extended beyond this load. The elastic stiffness constant (C_{11}) was calculated using Wooster's empirical relation as (Wooster, 1953).

$$C_{11} = H_V^{\,7/4} \quad (3)$$

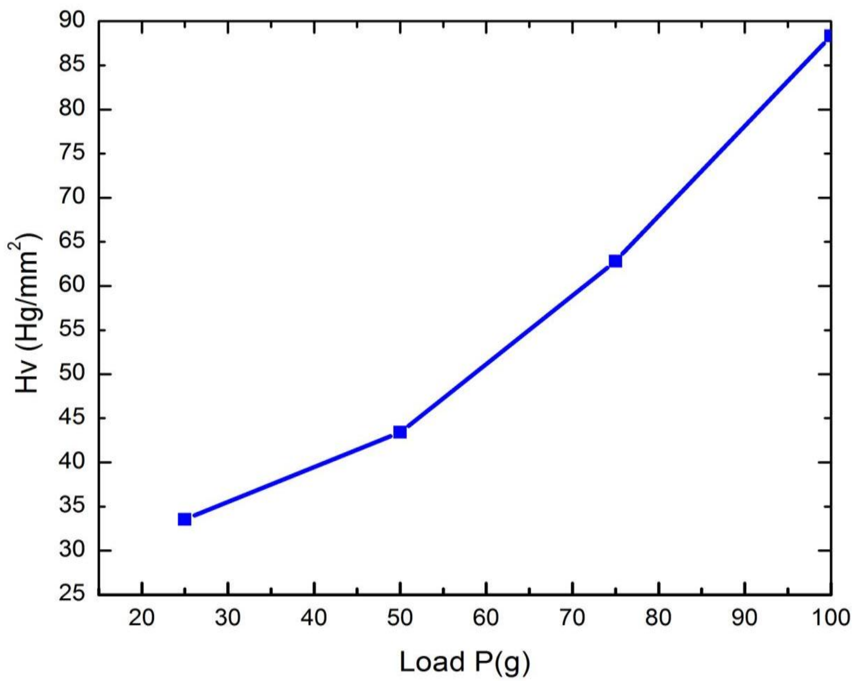

Figure 3. Variation of the microhardness number H_V with load.

RESULTS AND DISCUSSION

Vicker's microhardness test

Figure 3 shows the variation of H_V as a function of applied loads, ranging from 25 to 100 g. It is clear from the figure that H_V increases with an increase in the load. The Mayer's index number was calculated from the Mayer's law, which relates the load and indentation diagonal length.

$$P = kd^n \quad (4)$$

$$\log P = \log k + n \log d \quad (5)$$

where *k* is the material constant and *n* is the Mayer's index (or work-hardening coefficient). The above relation indicates that H_V should increase with the increase in P if n > 2 and decrease with P when n < 2. The '*n*' value was determined from the plot of log P *vs* log d, as shown in Figure 4. The slope of the plot of log P versus log d will give the work hardening index (n) which is found to be 3.50. The material glycine lithium chloride is confirmed with large amount of mechanical strength which is better for device fabrications. According to Onitsch (1950) the value of '*n*' is less than 2 for hard materials and more than 2 for soft ones. Thus, glycine lithium chloride crystals belong to the soft-material category. Since glycine lithium chloride is having moderately higher value of hardness number, the material is found to be suitable for device fabrications.

The elastic stiffness constant (C_{11}) was calculated by Wooster's empirical relation. The calculated stiffness constant for different loads was tabulated (Table 1). The crack length is measured from the centre of indentation mark to the crack end. Here, the crack length (*l*) is the average of two crack lengths for each indentation. Resistance to fracture indicates the toughness of material (Jain et al., 1994). The fracture mechanics of the indentation process gives an equilibrium relation for a well-developed crack extending under the centre loading condition;

$$K_c = \frac{P}{\beta_0 l^{3/2}}, l \geq \frac{d}{2} \quad (6)$$

where β_0 is the indenter constant, equal to 7 for the Vicker's diamond pyramid indenter (Lawn and Marshal, 1979) and other symbols have their usual meanings. For the glycine lithium chloride crystal, the value of K_c is found to be 2.84×10^4 Kg m$^{-3/2}$, 3.15×10^4 Kg m$^{-3/2}$, 15.16×10^4 Kg m$^{-3/2}$ and 27.69×10^4 Kg m$^{-3/2}$ at 25, 50, 75 and 100 g respectively.

Brittleness is another property, which affects the mechanical behaviour of a material, and is expressed in terms of the brittleness index (B_i) as.

$$B_i = \frac{H_V}{K_c} \quad (7)$$

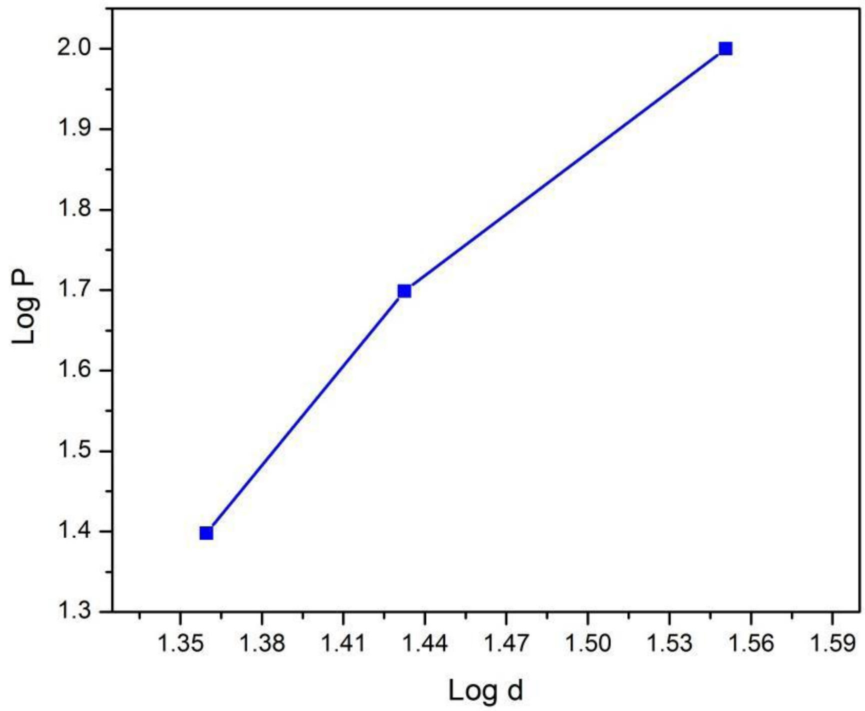

Figure 4. log P vs. log d.

Table 1. Elastic stiffness constant of glycine lithium chloride.

Load P (g)	H_V (Kg/mm^2)	$C_{11 \times 10}{}^{14}$ Pa
25	33.55	4.67
50	43.40	7.33
75	62.80	14.00
100	88.35	25.46

The calculated values of B_i are found as 13.07 × 10^4 $m^{-1/2}$, 13.78 10^4 $m^{-1/2}$, 4.14 × 10^4 $m^{-1/2}$ and 3.19 × 10^4 $m^{-1/2}$ at 25 g, 50 , 75 and 100 g respectively.

Knoop microhardness test

Knoop hardness (H_K) was plotted against loads (P). The plot is shown in Figure 5. From this measurement, it is found that as the load increases the Knoop microhardness number also increases. From the Knoop microhardness measurements, the Young's modulus (E) of the crystal was calculated using the relation (Pal and Kar, 2005).

$$E = 0.45 H_K / (0.1406 - b/a) \quad (8)$$

where H_K is the Knoop microhardness value at a particular load, and 'b' and 'a' are the shorter and longer Knoop indentation diagonals respectively. The calculated Young's Modulus is 1.53 ×10^{10} Nm^{-2}.

Conclusion

The Vicker's and Knoop microhardness studies were carried out on the grown glycine lithium chloride single crystal. The Vickers and Knoop hardness numbers were calculated for the glycine lithium chloride single crystal, by the application of load and the hardness numbers were found to increase with an increase in the load. The value of the Mayer's index number is found as 3.50, which proves that glycine lithium chloride falls in the soft-material category. The calculation of the stiffness constant (C_{11}) reveals that the binding force between the ions is quite strong. The Young's modulus was calculated from the diagonal lengths of the Knoop indentation.

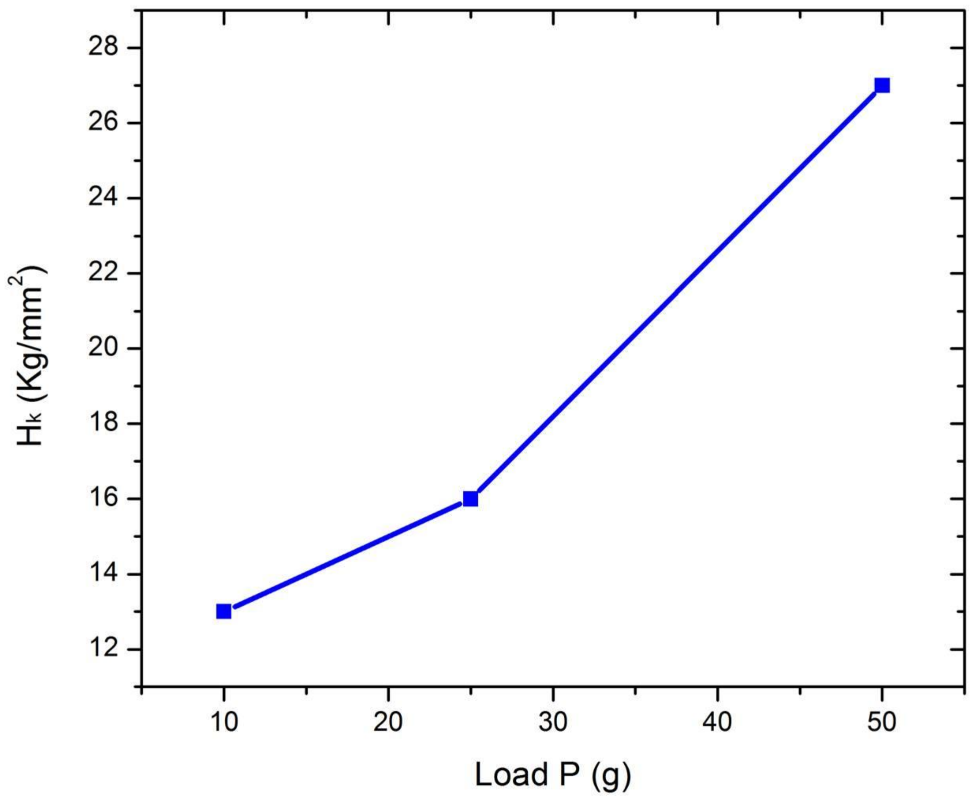

Figure 5. Variation of the Knoop microhardness with load.

ACKNOWLEDGEMENTS

The authors thank the Management of Sree Sastha Institute of Engineering and Technology, Chembarambakkam, Chennai -600123 for their encouragements throughout this work. One of the authors S.Suresh, thanked R.Varatharajan, Principal, Sree Sastha Institute of Engineering and Technology, Chembarambakkam, Chennai -600123, for spending his precious time in scientific discussions, for his personal involvement, innovative ideas, and critical and valuable suggestions throughout the preparation of this paper.

REFERENCES

Ashby NA (1951). The factor of hardness in metals. New Zealand Engineering. J. Nuclear Eng. 6:33-34.

Desai CC, Rai JL (1983). Microhardness studies of SnI_2 and SnI_4 single crystals. Bull. Mater. Sci. 5:453.

Onitsch EM (1950). The present status of testing the hardness of materials. Microscope. 95:12.

Jain A, Razdan AK, Kotru PN, Wanklyn BM (1994). Load and directional effects on microhardness and estimation of toughness and brittleness for flux-grown $LaBO_3$ crystals. J. Mater. Sci. 29:3847.

Ke YL, Dong FX (2009). Hardness of materials: studies at levels from atoms to crystals. Chinese Sci. Bull. 54:131-136.

Ke YL, Dong FX (2010). Hardness of group IVA and IVB nitrides. Physica Scripta, T139:014073.

Lawn BR, Marshal DB (1979). Hardness, Toughness and Brittleness, an Indentation Analysis. J. Am. Ceram. Soc. 62:347.

Mott BW (1958). Hardness of Butter, Influence of Season and Manufacturing Method Micro indentation hardness testing, J. Dairy Sci. 41:360-368.

Pal T, Kar T (2005). Studies of Microhardness anisotropy and Young's modulus of nonlinear optical crystal l-arginine hydrochlorobromo monohydrate. Mater. Lett. 59:1400.

Shaw MC (1973). The Science of Hardness Testing and its Research Application, Ed. By Westbrook J.H. and Condrad H, ASM. Ohio, pp. 1-11.

Smith RL, Sandland GE (1923). "An Accurate Method of Determining the Hardness of Metals with Reference to those of a High Degree of Hardness". Proc. Inst. Mech. Eng. 1:623-641.

Stillwel CW (1938). Crystal Chemistry, McGraw Hill, New York.

Westbrook JH, Conrad H (1971). The Science of Hardness testing and its Research Applications, American Society for Metals, Ohio.

Wooster WA (1953). Physical properties and atomic arrangements in crystals, Reports on Progress in Physics. Rep. Prog. Phys. 16:62.

Xingtao KL, Fangfang WZ, Dongfeng X (2008). Electronegativity identification of novel superhard materials, Phys. Rev. Lett. 100:235504.

academicJournals

Vol. 8(39), pp. 1898-1906, 23 October, 2013
DOI: 10.5897/IJPS2013.4027
ISSN 1992 - 1950 © 2013 Academic Journals
http://www.academicjournals.org/IJPS

International Journal of Physical Sciences

Full Length Research Paper

Comparative performance of Raman-SOA and Raman-EDFA hybrid optical amplifiers in DWDM transmission systems

V. Bobrovs, S. Olonkins, A. Alsevska, L. Gegere and G. Ivanovs

Institute of Telecommunications, Riga Technical University, Azenes Str. 12, Rīga, LV-1048, Latvia.

Accepted 22 October, 2013

To combine the benefits and compensate for the drawbacks of different optical amplifier types, a hybrid amplifier can be composed. The authors consider two most frequently used hybrid amplifiers that can provide better performance: a semiconductor optical amplifier (SOA), and an erbium doped fiber amplifier (EDFA), both in combination with a distributed Raman amplifier (DRA). To compare performance of the hybrid amplifiers, the eye diagrams of detected signals were analyzed and the maximum transmission distances were found. The results obtained show that even under the conditions advantageous for a SOA-DRA hybrid, the EDFA-DRA combination will produce less distortions of the amplified signal.

Key words: Dense wavelength division multiplexing, hybrid amplifier, semiconductor optical amplifier.

INTRODUCTION

During the last decade the evolution of available multimedia services and the rapid growth in the number of worldwide internet users has given rise to the demand for high capacity networks; this, in turn, causes a major shift in the evolution of optical transmission systems. Nowadays, one on the most typical solutions for raising transmission capacity is the use of wavelength division multiplexing (WDM), where different optical signal frequencies are used in order to achieve simultaneous transmission of a definite number of optical channels over a single fiber. It is also important to maintain the required level of system performance over a longer transmission distance. Such multichannel systems – in addition to linear effects such as optical attenuation and chromatic dispersion – are highly sensitive to the fiber non-linearity, the presence of which may result in serious signal distortion thus causing a dramatic degradation of a system's performance. Still, the effect that puts the greatest limitations on the transmission distance is the optical signal attenuation (Bobrovs et al., 2011a, b; Olonkins et al., 2012).

To compensate for optical signal attenuation, two ways are known: the use of signal repeaters and optical signal amplification. The former solution is not the best for WDM systems, because it requires demultiplexing, conversion, processing and regenerating of signals of all 16 channels; therefore, it is too complex and expensive (Agrawal, 2002). At the same time, by amplifying the optical signal we raise its power during transmission without conversion into any other form; the method is therefore simpler and much cheaper than those using repeaters. In some of the types of optical amplifiers optical signal gain is provided

*Corresponding author. E-mail: vjaceslavs.bobrovs@rtu.lv, Tel: +371 27896246.

Abbreviation: Dense wavelength division multiplexing, **DWDM;** hybrid amplifier, **HA;** semiconductor optical amplifier, **SOA;** erbium-doped fiber amplifier, **EDFA;** distributed Raman amplifier **DRA;** nonlinear optical effects, **NOEs;** amplified spontaneous emission, **ASE.**

through stimulated emission, and in the others fiber nonlinearity is used.

In the amplifier medium also a spontaneous emission also occurs, which is amplified together with the transmitted signal. This results in the amplified spontaneous emission (ASE) noise, which in some cases can seriously limit the total transmission distance.

In WDM transmission systems the following types of optical amplifiers are used: semiconductor optical amplifiers (SOAs), doped fiber amplifiers (DFAs), discrete (lumped), and distributed Raman amplifiers (LRAs and DRAs). In the nearest future, parametrical amplifiers will also become available for multichannel systems. Each of these amplifier types has its own benefits and drawbacks. The main problem with SOAs is that they produce the largest amount of ASE and their gain dynamics can cause serious signal distortions. The DFAs can provide signal amplification with considerably less signal impairments than in the SOA case; however, their gain spectrum is highly frequency-dependent due to the characteristics of the doped material. Raman amplifiers can provide the most noiseless amplification; in this case the gain spectrum can easily be changed by varying the number of pumps and their frequencies, while to achieve a high enough gain a very powerful pump is needed, the use of which is not economically reasonable (Agrawal, 2002). To compensate for the drawbacks and combine the benefits of different amplifiers, these can be used together, forming a hybrid amplifier. In modern transmission systems a great variety of such combinations can be used; we, therefore, decided to carry out research on the hybrid amplifiers.

INVESTIGATION ON THE AMPLIFIER TYPES

As already mentioned, for amplification of optical signals the stimulated emission is used. In SOAs, the electrical energy is applied as a pump to achieve the population inversion, and amplification is achieved via the stimulated recombination luminescence. The spontaneous carrier lifetime in the active region of material is times smaller than in other amplifier types, so it is highly important for the SOA to work close to the saturated mode in order to keep the ASE level low. The amplifier gain dynamics, which is determined by the quick carrier recombination lifetime, for SOAs is faster than in other types of amplifiers. Consequently, the amplifier will respond relatively quickly to the changes in the input optical signal power. This may cause severe signal distortions, especially in multichannel systems (Connely, 2004). Because pulses from different channels are amplified simultaneously, the pulse belonging to one channel may drain the total higher energy level population, thus resulting in smaller optical gain for a pulse that corresponds to another channel; this process is called cross-gain modulation (Agrawal, 2002). The main advantages of using SOAs are their broad amplification bandwidth (that is, -3 dB up to 70 nm) and relatively low price (Agrawal, 2002).

DFAs make use of rare-earth elements for doping some silica fibers during the manufacturing process. For this purpose, many different rare-earth elements can be used (erbium, thulium, neodymium, ytterbium, chromium etc.) (Cheng and Huang, 2013). The most usable element is erbium, because it allows optical amplifiers to operate in the C-band, (that is from 1530 to 1565 nm). In order to achieve efficient pumping in erbium- doped fiber amplifiers (EDFAs) the 980 and 1480 nm semiconductor lasers are applied, while population inversion is achievable using co-propagating, counter-propagating and bi-directional pumps. The gain spectrum of EDFAs is determined by the molecular structure of the doped fiber, and is strictly wavelength-dependent. The main disadvantage of EDFAs is that their wavelength-dependent gain spectrum bandwidth is only about 40 nm; besides, it is not flat. On the other hand, it determines amplification of individual channels when a WDM signal is amplified, so no cross-gain saturation occurs. Due to a relatively long spontaneous carrier lifetime in silica fibers, this allows achieving high gain for a weak signal with low noise figure, which represents the difference in signal-noise ratio at the input and output of the device under consideration (Agrawal, 2002). This is the main reason why the EDFAs are most frequently used for optical amplification.

Nowadays, Raman amplifiers are being deployed in most of the new long-haul and ultra-long haul fiber optic transmission systems, placing them among the first widely commercialized nonlinear optical devices in telecommunications (Islam, 2004a). In Raman amplifiers a small signal gain arises from stimulated Raman scattering (SRS) – the energy transfer from a powerful pumping optical beam to the amplified signal. In silica fibers, the peak amplifications correspond to the signal frequency that is ~ 13.2 THz lower than the pumping one; this frequency difference is called the Stokes shift. Such downshift is defined by the energy of optical phonons which represent the vibration mode of medium (Islam, 2004a). Despite the fact that the spontaneous Raman scattering spectrum is broad, the coherent nature of the process implies that the small signal radiation becomes coherently amplified by the SRS. The main advantage of Raman amplifiers is that the gain spectrum is very broad, and its shape can be changed by varying the number of pumps and their wavelengths (Mustafa et al., 2013). The relatively low noise figure of Raman amplifiers also is a significant benefit. It is these two aspects that make Raman amplifiers the main component of hybrid amplifiers, as they can be used to enhance the gain of a particular amplifier, and to broaden and equalize the gain spectrum, adding very little noise to the amplified signal. The main disadvantages of Raman amplifiers are the poor pumping efficiency at lower signal power (Tragarajan and Ghatak, 2007), and the use of expensive powerful lasers capable of delivering great powers into single-mode fibers.

In the systems with optical amplification the intensity of amplified signal can reach the level high enough to cause fiber nonlinearity, which may result in serious inter-channel crosstalk, thus also in a dramatic decrease in the transmission quality. For the systems that are highly sensitive to fiber nonlinearity (such as dense WDM (DWDM) systems with equal channel spacing) it is very important to keep track of the inter-channel crosstalk produced by the four-wave mixing (FWM). Indeed, such FWM induces spectral components with frequencies that may coincide with those of transmitted signal channels, thus limiting the amplifier gain for which the required quality of service is maintained. In such cases, the ASE and other amplifier-produced signal distortions may have a great impact on the maximum achievable transmission distance. This means that SOAs are not the preferable type of optical amplifier for such a system.

With the mentioned gain limitations the Raman amplifiers may cause too much inter-channel crosstalk, while the DFAs also can raise the signal intensity level significantly enough to cause inter-channel crosstalk, and, due to their gain- frequency dependence, they may not provide equivalent amplification for all of the system's channels so this needs to be equalized. The use of a SOA-DRA or, alternatively, of an EDFA-DRA hybrid may help to overcome these problems (Islam, 2004b).

In general, two types of hybrid amplifiers are known: the wideband hybrid amplifier (WB-HA) and the narrowband hybrid amplifier (NB-HA) (Islam, 2004b). In the former a wider band for the gain is obtained using combinations of different amplifier types, while in the NB-HA such combinations are meant for obtaining a compound with lower ASE-produced noise and higher gain of the amplified signal.

Raman amplifiers are an essential component of hybrid amplifiers. Obviously, hybrid SOA-EDFAs can be used in the cases where it is necessary to widen the gain spectrum of an EDFA, which could be done applying the most cost-effective solution (Zimmerman and Spiekman, 2004); however, such a combination generates a greater amount of ASE than in the cases of EDFA-DRAs or SOA-DRAs. This significantly affects the total system performance in the case of a nonlinearity-sensitive transmission system, where, due to the limitations on signal amplification caused by nonlinearity, the received optical power penalty plays a great role as it affects the receiver's sensitivity needed for achieving a definite bit error rate (BER). Therefore, normally it is not applied in long haul or DWDM systems. Our previous studies show that the noise figure of Raman amplifiers is much lower than that of EDFAs, and definitely lower than in the cases where SOAs are used. So the best way to achieve a higher gain with lower noise figure or a wider amplification band is to use a SOA or an EDFA in combination with a distributed Raman amplifier (DRA). For this purpose, we can also use another type Raman amplifiers – the discrete ones (Islam, 2004b); however, due to a small effective area and a high nonlinearity coefficient of the HNLFs and dispersion compensating fibers employed as the amplifier medium in LRAs, the discrete RAs generate a multitude of nonlinearity-related distortions in the cases when the intensity level of a weak signal to be amplified is relatively high.

Therefore, it is unclear whether SOA-DRA or EDFA-SOA combinations would provide better system performance in the case where the impact of fiber nonlinearity is strong. Our main goal was therefore to find out which of these combinations can ensure good enough signal amplification with less distortions (that is, with longer transmission distance) and without loss in the operational quality of a nonlinearity-sensitive transmission system.

SIMULATION SCHEME AND MEASUREMENT TECHNIQUE

Here, we will describe the simulation and measuring schemes used for performance estimation of hybrid optical amplifiers. To compare the performance of SOA-DRA and EDFA-SOA combinations a quality-characterizing parameter is to be evaluated. In our case, the most efficient way to assess the quality of transmission is to analyze the eye diagrams, which show patterns of the electrical signal after detection, and to evaluate BER values of the transmitted signal as a parameter featuring best the signal distortions arising during transmission. To estimate the transmitted signal distortions caused by fiber nonlinearity, we will observe its optical spectrum, while the level of ASE-generated noise will be assessed by noise figures.

To obtain the experimental results we needed a strong mathematical tool. For this purpose, the OptSim 5.2 simulation software was chosen, so that this all-optical network simulator can handle complex simulations and introduce high-accuracy results without imposing high requirements on the relevant hardware. This simulation tool uses the split-step method to perform integration of the fiber propagation equation (OptSim 5.2 User Guide, 2010):

$$\frac{\partial A(t,z)}{\partial z} = \{L + N\} A(t,z) \tag{1}$$

where A(t,z) is the optical field, L is the linear operator (for calculation of such linear effects as attenuation and dispersion), and N is the nonlinear operator (accounting for fiber nonlinearity).

The calculation is done dividing the whole optical link (fiber) into Δz-long spans, and deriving the L and N operators separately (Zimmerman and Spiekman, 2004). Two variants of the split-step method are applied: time domain split step (TDSS) and frequency domain split step (FDSS). These two differ only in the way the L operator is calculated: in the TDSS method – in the time domain, while in the FDSS – in the frequency domain. The nonlinear operator in both cases is obtained in the time domain. The former method gives highly precise results, however it is difficult to implement. The FDSS is easier to implement, but intrinsic errors (that decrease dramatically the precision of the results (OptSim 5.2 User Guide, 2010) can arise during the calculation process. Therefore, for our simulation the TDSS method was chosen.

For studying the signal distortions caused by hybrid amplifier a 10 Gbps 16- channel DWDM transmission system was designed,

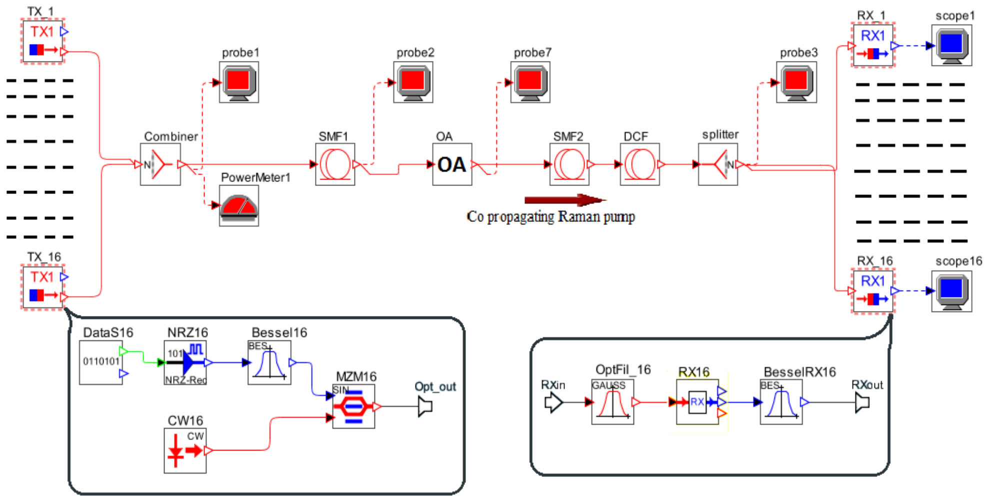

Figure 1. Simulation scheme of a 10 Gbit/s 16 channel DWDM system.

with the non-return-to-zero (NRZ) encoding, the on-off keying (OOK) intensity modulation format (less tolerant to the influence of fiber nonlinearity than advanced modulation formats (Bobrovs et al., 2011c), and a 50 GHz channel spacing. Such system configuration was chosen to purposefully to cause the Kerr effect in order to impact the amplified signal. This nonlinear effect (arising in systems with equal and relatively small channel spacing) produces strong inter-channel crosstalk, thus limiting the maximum intensity level of the transmitted signal and, therefore, the total amplification. In such a system the amplifier-produced signal impairments will directly influence the achievable transmission distance. Therefore it is easier to assess the performance of the amplifiers by comparing the achieved transmission distances. The simulation scheme comprising three main blocks: the transmitter block, the optical link and the receiver block, are shown in Figure 1.

The transmitter block consists of 16 NRZ-OOK externally modulated channel transmitters, each of them operating at its own frequency in the range from 193.05 to 193.8 THz. Each transmitter contains a pulse pattern generator (PPG), an NRZ driver, an electrical filter, a continuous wave (CW) laser, and a Mach-Zender's modulator. The continuous optical signal is externally modulated by NRZ-coded electrical pulses via an electro-optical MZM. Then all of the 16 generated optical signals are combined and transmitted through the optical link.

The signal first overcomes 72 km of a single mode fiber (SMF) with 0.2 dB/km attenuation and 16 ps/nm/km chromatic dispersion. The SMF length is dictated by the required optical signal power at the input of the optical amplifier, which is very important due to its saturation effect – especially when SOA is used. For an EDFA this parameter is also relevant, but it has been optimized for the semiconductor amplifier (due to the high level of noise produced by SOA and its gain dynamics). The weak signal power level for each channel at the amplifier input is around -22.4 dBm. Then the signal is amplified by an in-line SOA or an EDFA.

The two hybrid amplifiers (SOA-DRA and EDFA-DRA) will be compared as in-line amplifiers, because such amplifiers not only cause signal impairments and raise the intensity level significantly enough to cause fiber nonlinearities, but also amplify the nonlinearity-caused signal distortions accumulated during transmission. This makes the requirements for the total acceptable amount of amplifier noise stricter.

The SOA pumping current is optimized in order to minimize the amplifier-produced signal impairments. The EDFA parameters are chosen in such a manner that its gain spectrum irregularities would be easy to compensate with a single Raman amplifier pump, keeping in mind the total gain limitation caused by FWM. Then the amplified signal enters another SMF where it is amplified by a low-power DRA, the power of which allows for achievement of the maximum signal gain without causing too much nonlinearity-produced distortions. The length of this second SMF is variable in order to obtain the maximum transmission distance. At the end of optical link the signal enters a dispersion compensation fiber (DCF), the length of which will also be varied so as to find a balance between the dispersion compensation and the DCF insertion loss. After propagating through the DCF, the optical signal enters the receiver block. It is divided among 16 receivers, where the optical signal is filtered, detected and converted into electrical current. The DCF attenuation at 1550 nm is 0.55 dB/km, and the dispersion at this wavelength is -80 ps/nm/km.

RESULTS AND DISCUSSION

We will focus our attention on the results obtained with the simulation scheme described above. Besides, the amplifier optimization results will be presented, which may provide a good basis for estimating the cause of amplifier performance limitations. As already mentioned, in order to estimate the system performance the eye diagrams should be analyzed. The eye diagram is a powerful time domain tool for assessing the quality of the received signal and for analyzing the signal distortions. It can give much information on the timing jitter, the system rise time, and the signal amplitude distortions (Bobrovs and Ivanovs, 2008). First, we will discuss the configurations of SOA-DRA and EDFA-DRA allowing the maximum transmission distance to be achieved. The active layer parameters of the SOA and its other geometrical and material parameters were found in Singh and Kaler (2007), where a semiconductor optical amplifier was optimized for a similar system. They are specified in Table 1.

Table 1. The SOA parameters.

Parameter	Value	Unit
Amplifier length	750	µm
The active layer width	2	µm
The active layer thickness	0.2	µm
Confinement factor	0.41	µm
Transparency carrier density	$1.5 \cdot 10^{18}$	cm^{-3}
Differential gain constant	$2.1 \cdot 10^{-16}$	cm^{2}
Carrier recombination time	0.3	Ns
Input and output coupling losses	3	dB

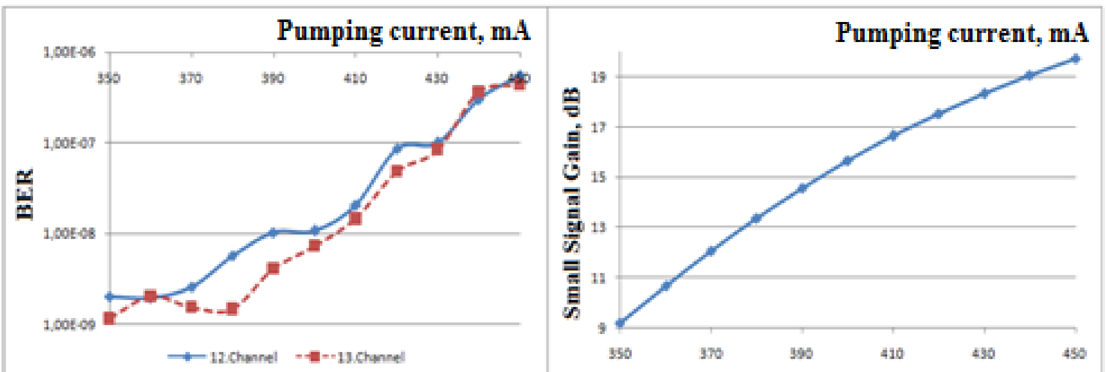

Figure 2. BER values at the output of SOA for channels 12 and 13 of the transmitted signal with gain compensation vs. pumping current (left); the optical gain vs. the pumping current (right).

The current to be used for pumping in the semiconductor amplifier should be chosen from the considerations of achieving the maximum amplification with the minimum noise. With this purpose in mind, we found the BER level in two channels for the signal before and after amplification at different current values (from 350 to 450 mA). The channels were purposely chosen with the highest and the lowest optical power level at the SOA output – the 12th and the 13th channel, respectively. It is important to note that in order to avoid the impact of the amplifier gain on the BER values of the two channels, the optical signal was intentionally attenuated, so that a weak signal's gain would be completely compensated. We also obtained the dependence of the amplified signal gain on the pumping current and its increase with every additional 10 mA. The results are shown in Figure 2.

The BER value of the 12th channel at the amplifier input was 2.04•10-9, and of the 13th channel – 9.96•10-10, that is, lower, despite the fact that the optical power of the 12th channel is slightly higher. This can be explained by the closeness of the 12th channel to the center of the transmitted signal spectrum, which increases (also slightly) its inter-channel crosstalk. For the pump current starting from 380 mA, the BER values of the two channels under consideration experience a significant increase. This evidences that for the pump current values over 370 mA the amount of amplifier-produced signal distortions starts to grow. Therefore, we took the 370 mA pumping current as optimal for this system.

In Figure 2 it could be seen that with increase in the pumping current the amplifier gain increment is becoming smaller. This evidences that the amplifier slowly reaches the maximum level of population inversion; thus, due to the short spontaneous carrier lifetime, the generated ASE also experiences an increment with the increase in pumping current. For its value of 370 mA the SOA provides a small signal gain of 12.1 dB. The fact that SOAs provide a very broad gain bandwidth is confirmed by another fact – that the difference in the optical gain values for all 16 channels is only 0.02 dB. The rest of the amplifier gain will be provided by a noiseless distributed Raman amplifier.

For the hybrid EDFA-DRA we have chosen a bi-directionally pumped EDFA, with 980 nm co-propagating and 1480 nm counter-propagating pumps. In our earlier research such combination of pump wavelengths showed the best result from those for many single and multiple pump combinations. The pump powers were chosen with the purpose to make the gain spectrum irregularity of the

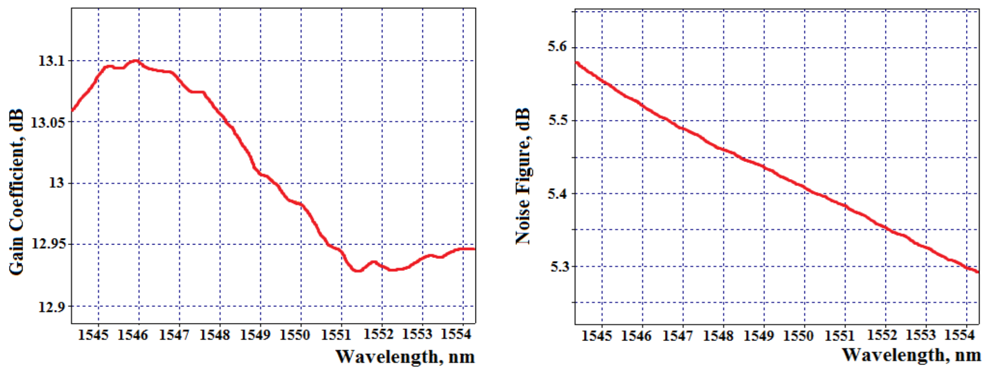

Figure 3. Gain spectrum (left) and noise figure (right) of the EDFA with 5 m long doped fiber and 10 dBm 980nm co-propagating and 16 dBm 1480 nm counter-propagating pumps.

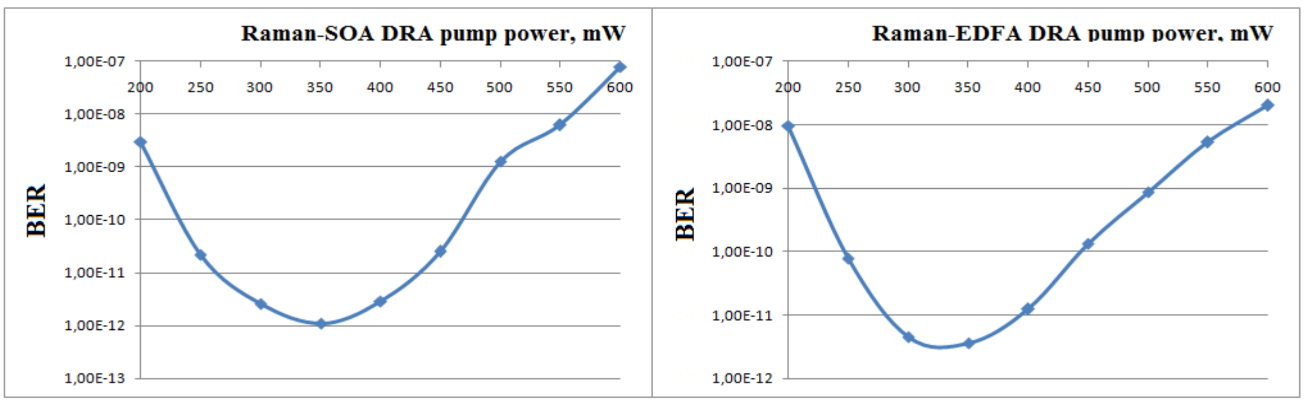

Figure 4. System's BER dependence on the power of a 1451.8 nm SOA-DRA (left) and EDFA- DRA (right) co-propagating pump.

EDFA easier to compensate with a single-pump Raman amplifier. In our case, the 16 channels occupy a ~ 6 nm bandwidth, in the limits of which a low-power single-pump DRA gain difference is < 0.5 dB. Taking this fact into account, we decided that a 5 m long doped fiber should be used for our EDFA, with the population inversion achieved using a combination of 10 dBm 980 nm co-propagating and 16 dBm 1480 nm counter-propagating pumps. The obtained gain spectrum and noise figure are shown in Figure 3, where the gain spectrum obtained for wavelengths from 1547 to 1553 nm varies from 12.93 dB to 13.1 dB. This but minor gain unevenness and the specific shape of the gain spectrum allowed us to conveniently equalize the obtained gain-wavelength dependence by applying a single-pump Raman amplifier. The noise figure obtained for the wavelengths under attention varies from 5.33 to 5.49 dB, which is rather a large increment for the EDFAs operating at high levels of population inversion. For the optimal amplifier configuration the noise figure close to 3 dB mark is achievable (Agrawal, 2002). So the EDFA configuration was not optimal, still the obtained noise figure is lower than the theoretical for a SOA.

After configuration of EDFA and SOA this procedure was carried out for the co-propagating Raman pump wavelengths and power in both cases. For the SOA-DRA hybrid the main requirement to the Raman pump was to ensure the minimum difference in the signal gain for all 16 channels. To achieve this, the center of the amplifier gain should coincide with the central wavelength of the transmitted signal. We found out that a 1451.8 nm pump is most suitable for this purpose. In the case of hybrid EDFA-DRA a pump is needed to ensure that the Raman amplification maximum coincides with the EDFA amplification minimum, which, in turn, corresponds to the wavelength of 1551.5 nm (or 193.23 THz frequency). It was found that to satisfy this criterion a 1453.1 nm pump is to be used.

To find the optimal pump power, we considered the BER values of all 16 channels and obtained the maximum one (further in the text the system's BER) and its dependence on the co-propagating pump power in both cases (Figure 4). From the results obtained it can be seen that in both cases for the pump power over 350 mW the amount of FWM-generated crosstalk exceeds the permissible value and seriously deteriorates the total

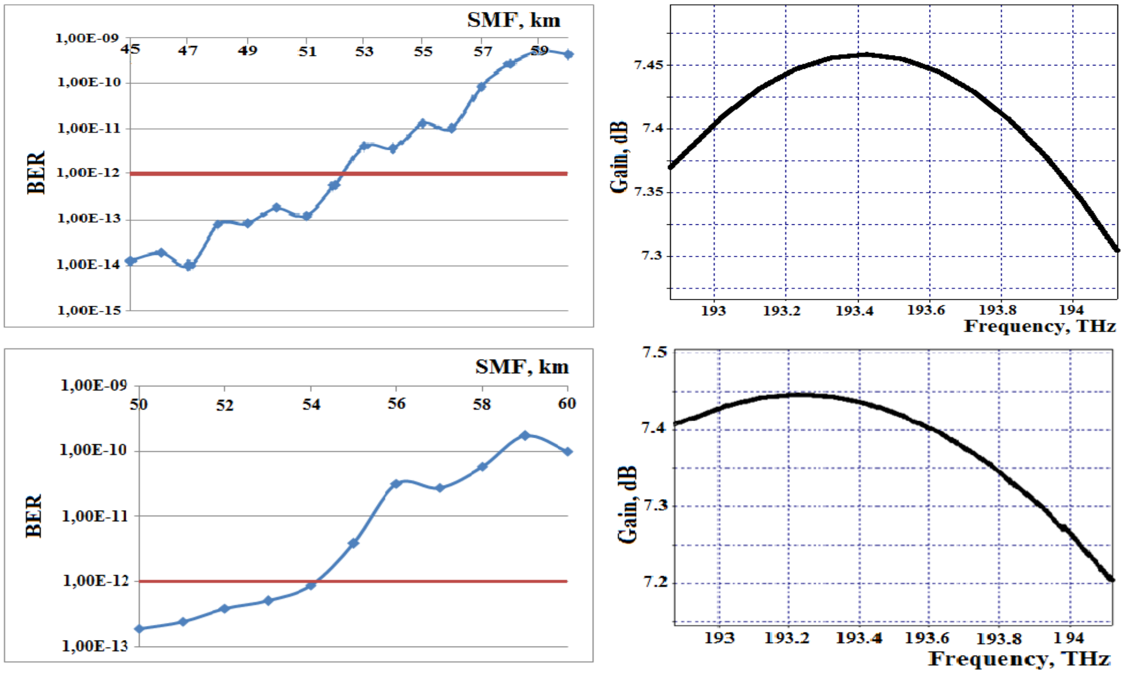

Figure 5. Dependences of the system's BER on the SMF length between the amplifier and the receiver block (left), and the DRA produced gain spectra (right) in the cases of SOA-DRA (above) and EDFA-DRA (below).

system performance. Therefore, 350 mW was found to be the most suitable value in the existing conditions. Since the SMF for DRA plays the role of amplifier medium, to obtain the total DRA gain we should first define the SMF length between the amplifier and the receiver block, thus also deriving the maximum transmission distance. For this, it is required to obtain the optimal DCF length, which, on the one hand, is determined by the total accumulated chromatic dispersion, while, on the other, is limited by the signal attenuation caused by DCF insertion. In both cases, the optimal DCF length was found to be 17 km. To find the maximum transmission distance we obtained the dependence of the system's BER on the sought-for SMF section length shown in Figure 5 along with the DRA gain spectra. The dependences shown in Figure 5 evidence that in the case of SOA-DRA the maximum SMF length between the amplifier and the receiver block providing the system's BER < 10-12 is 52 km, thus the overall transmission distance will be 124 km. For the EDFA-DRA based system this fiber length is 54 km, and the transmission distance – 126 km. It is important to add that we have obtained also the maximum transmission distance for the system in which no amplification was applied, and it was equal to 69 km. This means that the SOA-DRA combination was able to extend this distance by 55 km and the EDFA-DRA – by 57 km. The optical signal values at the receiver block input for the system with no amplification varied from -23.32 to -23.57 dBm, for the SOA-DRA based system from -21.78 to -21.44dBm, and for that with EDFA-DRA – from -21.31 to -21.05 dBm. To identify the factors that limit transmission in each of the three cases the eye diagrams of the channels with the worst BER were analyzed. These, together with the relevant inter-channel crosstalk, are shown in Figure 6.

As was expected, in the case with no amplification the main limitation factor is the optical signal attenuation. It also can be seen that even without amplification the optical signal intensity is high enough to initiate FWM, and the produced minor inter-channel crosstalk also affects the BER value. From the eye diagram of the 7th channel of the EDFA-DRA based system it can be seen that the FWM produced inter-channel crosstalk is the main limiting factor for transmission, since the FWM harmonics are clearly seen on the level of logical "1", and the critical BER value was reached with a higher level of the detected signal power than in the other two cases. For the SOA-DRA based system this inter-channel crosstalk is also quite high, though lower than in the case with EDFA-DRA, due to ~ 0.8 dB difference in the amplification in both cases. Still, the BER limit was reached at a shorter transmission distance, and not due to the mentioned difference, because the level of the detected signal was high enough to ensure the required quality of transmission. If we compare the optical signal power levels at the input of the receiver block, it can be seen that the average difference is ~ 0.4 dB, while the difference in the amplification is ~ 0.8 dB. Therefore it is clear that the SOA produces more ASE noise than the

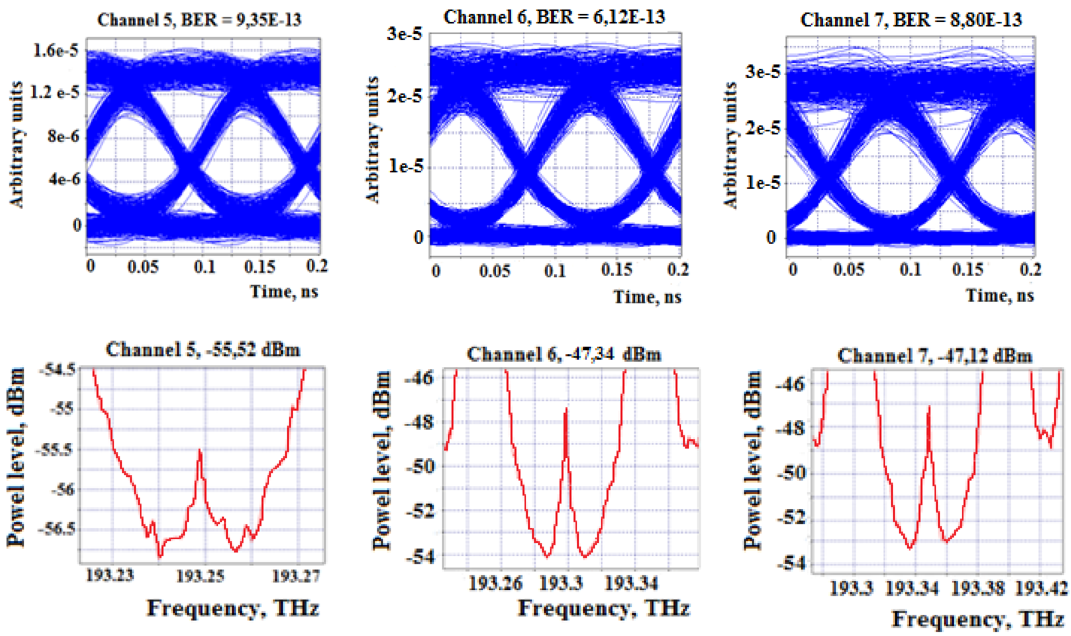

Figure 6. Eye diagrams for the channels with the worst BER (above) in the system with no amplification (left), with SOA-DRA (center), and with EDFA-DRA (right); the inter-channel crosstalk in the corresponding channels (below).

EDFA, which, in addition to the inter-channel crosstalk, increases the detected signal power penalty at the receiver.

Conclusions

Based on the results obtained in this work, the following conclusions can be drawn:

1. The fiber nonlinearity in the implemented 16-channel DWDM transmission system has been found to exert a strong influence on the quality of transmission, which allowed the performance of narrowband SOA-DRA and EDFA-DRA hybrid amplifiers to be compared.
2. Testing the amplifiers under severe conditions has given a clear view on the amplified signal distortions. The parameters of SOA were adjusted so that it would produce higher amplification with less signal distortions. It was observed that increasing the SOA pumping current (from 370 mA on) leads to a signal's BER growing after amplification, which points to greater signal distortions generated by SOA.
3. Implementation of hybrid amplification can provide more equal gain for all channels of the system under attention. In the case of the EDFA-DRA solution the parameters of the EDFA were adjusted to obtain the gain spectrum which could easily be equalized by a single-pump Raman amplifier. The introduced EDFA configuration ensured 0.17 dB gain difference among all 16 channels, but after supplementing the EDFA with a DRA we obtained the gain spectrum with only 0.05 dB maximal difference in amplification.
4. Even a non-optimally configured EDFA produces less signal distortions than the SOA. The input signal power was adjusted specially for the SOA, thus the EDFA was not optimally configured; still the EDFA-DRA hybrid amplifier showed better results and provided transmission over a longer optical link than the SOA-DRA (126 and 124 km, respectively). The SOA-DRA provided an average gain of 19.6 dB, and the EDFA-DRA – of 20.4 dB.
5. Since the EDFA generated less signal distortions, the EDFA-DRA solution ensured better quality of amplification than the SOA-DRA. In both cases, the main factor that limited transmission was the FWM-produced inter-channel crosstalk, with the DRA pumping power being the same. So the difference in the total transmission quality can be explained only by the performance of the SOA and the EDFA. In the case of SOA-DRA the total amplification was slightly lower, thus also lower inter-channel crosstalk could be expected. Still, the non-optimally configured EDFA-DRA showed better results. This can be explained by heavier signal distortions that those produced by SOA, even though it was configured in a manner to obtain more gain with less noise.

So it is clear that even though the gain spectrum of the EDFA can be quite uneven, the EDFA-DRA hybrid can ensure better quality of transmission than the SOA-DRA one, even in the conditions favorable for the latter. Of course, if the signal power level at the input of amplifier was lower, also its fiber nonlinearity produced distortions would have been smaller, with much greater gain and longer transmission distance provided by both hybrid amplifiers. Still the results obtained give quite clear view on their performance. The main conclusion therefore is: despite greater signal distortions produced by SOA-DRA, due to the spectral limitations of EDFAs it still is the preference solution for broad coarse WDM (CWDM) transmission systems.

ACKNOWLEDGMENT

This work has been supported by the European Regional Development Fund in Latvia within the project Nr. 2010/0270/2DP/2.1.1.1.0/10/APIA/VIAA/002.

REFERENCES

Agrawal GP (2002). Fiber-optic communication systems. New York : John Wiley & Sons Inc. 546:226-260.

Bobrovs V, Ivanovs G (2008). Comparison of Different Modulation Formats and Their Compatibility With WDM Transmission System. Latv. J. Phys. Tech. Sci. 45(2):3-16.

Bobrovs V, Ivanovs G, Spolitis S (2011a). Realization of Combined Chromatic Dispersion Compensation Methods in High Speed WDM Optical Transmission Systems. Electronics Electrical Eng. 7:101-106.

Bobrovs V, Ivanovs G, Udalcovs A, Spolitis S, Ozolins O (2011b). Mixed Chromatic Dispersion Compensation Methods for Combined HDWDM Systems. IEEE CPS Proceedings, 6th Int. Conf. Broadband Wireless Computing, pp. 313-319.

Bobrovs V, Spolitis S, Udalcovs A, Ivanovs G (2011c). Schemes for Compensation of Chromatic Dispersion in Combined HDWDM Systems. Latv. J. Phys. Tech. Sci. 48(5):30-44.

Cheng WH, Huang YC (2013). 300-nm Broadband Chromium-Doped Fiber Amplifiers. OFC/NFOEC Technical Digest, OTh4C.4.

Connely MJ (2004). Semiconductor Optical Amplifiers. Dordrecht: Kluwer Academic Publishers, 169:127-132.

Islam MN (2004a). Raman Amplifiers for Telecommunications. New York: Springer, 298:1-39.

Islam MN (2004b). Raman Amplifiers for Telecommunications 2, New York: Springer, 730:413-424.

Mustafa FM, Khalaf AAM, Elgeldawy FA (2013). Multi-pumped Raman Amplifier for Long-Haul UW-WDM Optical Communication Systems: Gain Flatness and Bandwidth Enhancements. IEEE CPS Proc. 15th Int. Conf. Adv. Communication Technol. pp.122-127.

Olonkins S, Bobrovs V, Ivanovs G (2012). Comparison of Semiconductor Optical Amplifier and Discrete Raman Amplifier Performance in DWDM Systems. Electronics Electrical Eng. 7:133-136.

OptSim 5.2 User Guide (2010). RSoft design group Inc.

Singh S, Kaler RS (2007). Simulation and Optimization of Optical Amplifiers in Optical Communication Networks. Thapar University, India. Doctoral Thesis. 68-71.

Tragarajan K, Ghatak A (2007). Fiber Optics Essentials. New Jersey: John Wiley & Sons Inc. 242:151-160

Zimmerman DR, Spiekman H (2004). Amplifiers for the Masses: EDFA, EDWA, and SOA Amplets for Metro and Access Applications. J. Lightwave Technol. 22(1):63-70.

academicJournals

Vol. 8(39), pp. 1907-1922, 23 October, 2013
DOI: 10.5897/IJPS2013.4029
ISSN 1992 - 1950 © 2013 Academic Journals
http://www.academicjournals.org/IJPS

International Journal of Physical Sciences

Full Length Research Paper

Effects of heat absorption and chemical reaction on a three dimensional MHD convective flow past a porous plate

N. Ahmed and K. Kr. Das

Department of Mathematics, Gauhati University, Guwahati-781014, India.

Accepted 10 October, 2013

An attempt has been made to investigate the effects of heat sink and chemical reaction on a three dimensional Magneto hydrodynamics (MHD) convective flow with mass transfer of an incompressible viscous electrically conducting fluid past a porous vertical plate with transverse sinusoidal suction velocity. A magnetic field of uniform strength is assumed to be applied transversely to the direction of the main flow. The magnetic Reynolds number is considered to be small that induced magnetic field can be neglected. The governing equations are solved by regular perturbation technique. The expression for velocity field, temperature field, species concentration, current density, the skin friction, Nusselt number and Sherwood number at the plate are obtained in non dimensional forms. The effect of Hartman number, chemical reaction parameter, heat sink parameter on the velocity field, zeroth order skin friction and the amplitude of the first order skin friction, first order Nusselt number and the first order Sherwood number at the plate are discussed graphically. It is seen that chemical reaction and heat sink have significant effects on the flow and on the heat and mass transfer characteristics.

Key words: Three-dimensional convective flow, heat transfer, incompressible viscous fluid, wall shear stress, heat sink.

INTRODUCTION

The investigation of magneto hydrodynamics (MHD) convection with mass transfer problems in presence of transverse magnetic field have attracted the attention of a number of scholars because of its wide application in many branches of science and technology such as geophysics, astrophysics, plasma physics, missile technology, etc. Engineers employ MHD principles in the design of heat exchangers, pumps and flow meters, thermal protection, etc. From technological point of view, MHD convection flow problems are also very significant in the fields of stellar and planetary magnetospheres, aeronautics, chemical engineering and electronics. MHD is also stabilizing a flow against the transition from laminar to turbulent flow and in reduction of turbulent drag and suppression of flow separation. The application of MHD principles in medicine and biology are of paramount interest owing to their significance in biomedical engineering in general and in the treatment of various pathological states in particular. Applications in biomedical engineering include cardiac magnetic resonance imaging (MRI), electro cardio gram (ECG) etc. The principle of dynamo and motor is a classical example of MHD convection.

The problems of above phenomena of MHD convection have been studied by many authors. Ferraro and Plumpton (1966), Cramer and Pai (1973) and Sanyal and Bhattacharya (1992) are some of them. The problem of the convection flows arising in fluids as a result of

*Corresponding author. E-mail: saheel_nazib@yahoo.com or kishoredas969@yahoo.in

interaction of the force of gravity and density difference caused by simultaneous diffusion of thermal energy and chemical species have been investigated by Bejan and Khair (1985), Raptis and Kafousias (1982) and Ahmed et al. (2005).

The effect of three dimensional flow caused by the periodic suction perpendicular to the main flow when the difference between the wall temperature and free steam temperature gives rise to buoyancy force in the direction of the free steam on heat transfer characteristic was investigated by Ahmed and Sarma (1997), Singh et al. (1998) and Choudhury and Chand (2002). Recently Jain and Gupta (2006) have investigated the effect of transverse sinusiodal injection velocity distribution on three dimensional free convective Couette flow of a various incompressible fluid in slip flow regime under the influence of heat sink. An analytical solution to the problem of the three dimensional free convective flow of an incompressible viscous fluid past a porous vertical plate with transverse sinusoidal suction velocity taking into account the presence of species concentration was obtained by Ahmed et al. (2006).

In many times it has been observed that foreign mass reacts with the fluid and in such a situation chemical reaction plays an important role in chemical industry. Theoretical descriptions of non-linear chemical dynamics have been presented by Epstein and Pojman (1998) and Gray and Scott (1990). The effects of chemical reaction and mass transfer on MHD flow past a semi-infinite plate was analysed by Devi and Kandasamy (2000). The effects of mass transfer, Soret effect and chemical reaction on an oscillatory MHD free convective flow through a porous medium have been investigated by Ahmed and Kalita (2010).

In view of the importance of the combined effect of chemical reaction and heat absorption, it is proposed to study a problem of three dimensional MHD convective flows past a porous vertical infinite plate with chemical reaction and heat absorption. The infinite plate assumption is one such classical idealization of great practical importance. Although the flow over a flat plate is the simplest case of boundary layer development in external flow, yet its significance cannot be undervalued because of its relevance to numerous engineering applications. Several configurations such as flow over airfoils, turbine blades, ship hulls, etc. can initially be estimated as flow past flat plates (Scheme 1). The justification of considering the three dimensional flow is that most of the fluid flows that occur in nature are three dimensional. Of course we have chosen a simple model of a three dimensional flow caused by transverse sinusoidal suction velocity.

The objective of the present work is to investigate the effect of chemical reaction as well as heat sink on a three dimensional convective flow past a porous plate. Our work is a generalization to the work done by Ahmed and Sarma (2010).

BASIC EQUATIONS

The equations governing the steady motion of an incompressible viscous electrically conducting fluid in presence of a magnetic field are:

The equation of continuity: div $\vec{q} = 0$ (1)

The Gauss's law of magnetism: div $\vec{B} = 0$ (2)

The momentum equation:

$$\left(\vec{q}.\vec{\nabla}\right)\vec{q} = -\frac{1}{\rho}\vec{\nabla}p + \frac{\vec{J}\times\vec{B}}{\rho} + \nu\nabla^2\vec{q} + \vec{g} \quad (3)$$

The energy equation:

$$\rho C_p\left[\left(\vec{q}.\vec{\nabla}\right)\bar{T}\right] = k\nabla^2\bar{T} + \varphi + \frac{\vec{J}^2}{\sigma} + Q_0\left(\bar{T}_\infty - \bar{T}\right) \quad (4)$$

The species continuity equation:

$$\left[\left(\vec{q}.\vec{\nabla}\right)\bar{C}\right] = D_M\nabla^2\bar{C} + D_T\nabla^2\bar{T} + \bar{K}\left(\bar{C}_\infty - \bar{C}\right) \quad (5)$$

The Ohm's law: $\vec{J} = \sigma\left[\vec{E} + \vec{q}\times\vec{B}\right]$ (6)

We now consider the steady convective flow of an incompressible viscous electrically conducting fluid in presence of heat sink taking into account the species concentration and chemical reaction past a vertical porous plate with transverse sinusoidal suction velocity as mentioned earlier by making the following assumptions:

(i) All the fluid properties except the density in the buoyancy term are constant.
(ii) A magnetic field of uniform strength B_0 is applied transversely to the direction of the main steam.
(iii) The magnetic Reynolds number is so small that the induced magnetic field can be neglected.
(iv) The viscous dissipation and magnetic dissipation energy are negligible.
(v) $\bar{T}_w > \bar{T}_\infty$ and $\bar{C}_w > \bar{C}_\infty$.

We introduce a co-ordinate system $\left(\bar{x}, \bar{y}, \bar{z}\right)$ with X-axis vertically upwards along the plate, Y-axis perpendicular to it and directed into the fluid region and Z-axis along the width of the plate. Let $\vec{q} = \bar{u}\,\hat{i} + \bar{v}\,\hat{j} + \bar{w}\,\hat{k}$ be the fluid velocity at the point $\left(\bar{x}, \bar{y}, \bar{z}\right)$ and $B_0\,\hat{j}$ be the applied magnetic field, $\hat{i}, \hat{j}, \hat{k}$ being the unit vectors along +ve X-axis, Y-axis and Z-axis respectively. The suction velocity is taken as follows:

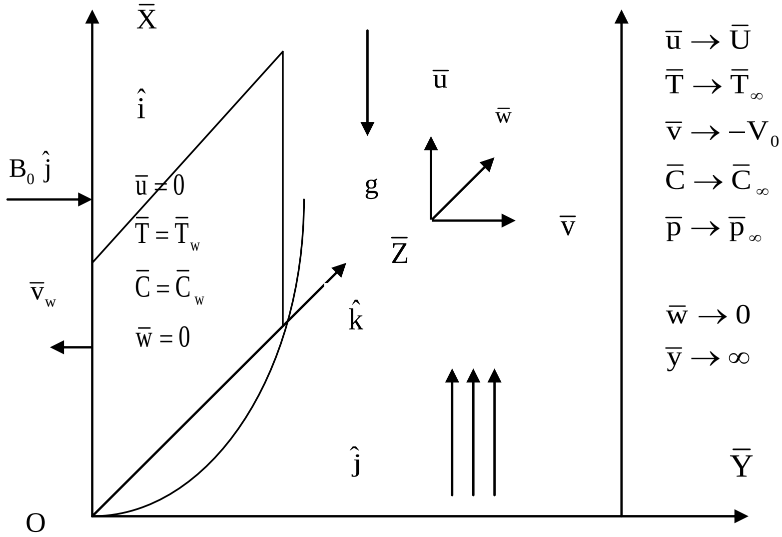

Scheme 1. Flow configuration.

$$\bar{v}_w(\bar{z}) = -V_0\left[1+\varepsilon\cos\frac{\pi\bar{z}}{L}\right] \quad (7)$$

which consists of a basic steady distribution $-V_0$ with a superimposed weak distribution $-\varepsilon V_0\cos\left(\frac{\pi\bar{z}}{L}\right)$. Since the plate is infinite in length in X-direction, therefore all the quantities except possibly the pressure are assumed to be independent of $\bar{x}$. With the foregoing assumptions and under usual boundary layer and Boussinesq approximation, Equations 1, 3, 4 and 5 are reduced to Equation of continuity:

$$\frac{\partial\bar{v}}{\partial\bar{y}}+\frac{\partial\bar{w}}{\partial\bar{z}}=0 \quad (8)$$

Momentum equations:

$$\bar{v}\frac{\partial\bar{u}}{\partial\bar{y}}+\bar{w}\frac{\partial\bar{u}}{\partial\bar{z}}=g\beta\left(\bar{T}-\bar{T}_\infty\right)+g\bar{\beta}\left(\bar{C}-\bar{C}_\infty\right)+\nu\left(\frac{\partial^2\bar{u}}{\partial\bar{y}^2}+\frac{\partial^2\bar{u}}{\partial\bar{z}^2}\right)+\frac{\sigma B_0^2}{\rho}\left(\bar{U}-\bar{u}\right) \quad (9)$$

$$\bar{v}\frac{\partial\bar{v}}{\partial\bar{y}}+\bar{w}\frac{\partial\bar{v}}{\partial\bar{z}}=-\frac{1}{\rho}\frac{\partial\bar{p}}{\partial\bar{y}}+\nu\left(\frac{\partial^2\bar{u}}{\partial\bar{y}^2}+\frac{\partial^2\bar{u}}{\partial\bar{z}^2}\right) \quad (10)$$

$$\bar{v}\frac{\partial\bar{w}}{\partial\bar{y}}+\bar{w}\frac{\partial\bar{w}}{\partial\bar{z}}=-\frac{1}{\rho}\frac{\partial\bar{p}}{\partial\bar{z}}+\nu\left(\frac{\partial^2\bar{w}}{\partial\bar{y}^2}+\frac{\partial^2\bar{w}}{\partial\bar{z}^2}\right)-\frac{\sigma B_0^2\,\bar{w}}{\rho} \quad (11)$$

Energy equation:

$$\bar{v}\frac{\partial\bar{T}}{\partial\bar{y}}+\bar{w}\frac{\partial\bar{T}}{\partial\bar{z}}=\alpha\left(\frac{\partial^2\bar{T}}{\partial\bar{y}^2}+\frac{\partial^2\bar{T}}{\partial\bar{z}^2}\right)+\frac{Q_0\left(\bar{T}_\infty-\bar{T}\right)}{\rho C_p} \quad (12)$$

Species continuity equation:

$$\bar{v}\frac{\partial\bar{C}}{\partial\bar{y}}+\bar{w}\frac{\partial\bar{C}}{\partial\bar{z}}=D_M\left(\frac{\partial^2\bar{C}}{\partial\bar{y}^2}+\frac{\partial^2\bar{C}}{\partial\bar{z}^2}\right)+D_T\left(\frac{\partial^2\bar{T}}{\partial\bar{y}^2}+\frac{\partial^2\bar{T}}{\partial\bar{z}^2}\right)+\bar{K}\left(\bar{C}_\infty-\bar{C}\right) \quad (13)$$

Equation 2 is satisfied by $\vec{B}=B_0\,\hat{j}$. The symbols are defined in the nomenclature. The relevant boundary conditions are:

at $\bar{y}=0$: $\bar{u}=0$, $\bar{v}=\bar{v}_w$, $\bar{w}=0$, $\bar{T}=\bar{T}_w$, $\bar{C}=\bar{C}_w$ (14)

at $\bar{y}\to\infty$: $\bar{u}=\bar{U}$, $\bar{v}=-V_0$, $\bar{w}=0$, $\bar{T}=\bar{T}_\infty$, $\bar{C}=\bar{C}_\infty$, $\bar{p}=\bar{p}_\infty$ (15)

We introduce the following non-dimensional quantities:

$$\left.\begin{array}{l} y=\frac{\bar{y}}{L},\ z=\frac{\bar{z}}{L},\ u=\frac{\bar{u}}{V_0},\ v=\frac{\bar{v}}{V_0},\ U=\frac{\bar{U}}{V_0},\ w=\frac{\bar{w}}{V_0},\ \theta=\frac{\bar{T}-\bar{T}_\infty}{\bar{T}_w-\bar{T}_\infty},\ Q=\frac{Q_0L}{\rho C_p V_0}, \\ \phi=\frac{\bar{C}-\bar{C}_\infty}{\bar{C}_w-\bar{C}_\infty}, P_r=\frac{\nu}{\alpha}, S_c=\frac{\nu}{D_M}, S_r=\frac{D_T\left(\bar{T}_w-\bar{T}_\infty\right)}{\nu\left(\bar{C}_w-\bar{C}_\infty\right)}, G_r=\frac{Lg\beta\left(\bar{T}_w-\bar{T}_\infty\right)}{V_0^2}, K=\frac{\bar{K}L}{V_0} \\ G_m=\frac{Lg\bar{\beta}\left(\bar{C}_w-\bar{C}_\infty\right)}{V_0^2}, M=\frac{\sigma B_0^2\nu}{\rho V_0^2},\ R_e=\frac{V_0L}{\nu},\ p=\frac{\bar{p}}{\rho\left(\frac{\nu}{L}\right)^2},\ p_\infty=\frac{\bar{p}_\infty}{\rho\left(\frac{\nu}{L}\right)^2} \end{array}\right\} \quad (16)$$

The non-dimensional forms of Equations 8, 9, 10, 11, 12 and 13

$$\frac{\partial v}{\partial y}+\frac{\partial w}{\partial z}=0 \quad (17)$$

$$v\frac{\partial u}{\partial y}+w\frac{\partial u}{\partial z}=G_r\,\theta+G_m\,\phi+\frac{1}{R_e}\left(\frac{\partial^2u}{\partial y^2}+\frac{\partial^2w}{\partial z^2}\right)+M R_e\left(U-u\right) \quad (18)$$

$$v\frac{\partial v}{\partial y}+w\frac{\partial v}{\partial z}=-\frac{1}{R_e^2}\frac{\partial p}{\partial y}+\frac{1}{R_e}\left(\frac{\partial^2v}{\partial y^2}+\frac{\partial^2v}{\partial z^2}\right) \quad (19)$$

$$v\frac{\partial w}{\partial y}+w\frac{\partial w}{\partial z}=-\frac{1}{R_e^2}\frac{\partial p}{\partial z}+\frac{1}{R_e}\left(\frac{\partial^2 w}{\partial y^2}+\frac{\partial^2 w}{\partial z^2}\right)-MR_e w \qquad (20)$$

$$v\frac{\partial \theta}{\partial y}+w\frac{\partial \theta}{\partial z}=\frac{1}{P_r R_e}\left(\frac{\partial^2 \theta}{\partial y^2}+\frac{\partial^2 \theta}{\partial z^2}\right)-Q\theta \qquad (21)$$

$$v\frac{\partial \phi}{\partial y}+w\frac{\partial \phi}{\partial z}=\frac{1}{S_c R_e}\left(\frac{\partial^2 \phi}{\partial y^2}+\frac{\partial^2 \phi}{\partial z^2}\right)+\frac{S_r}{R_e}\left(\frac{\partial^2 \theta}{\partial y^2}+\frac{\partial^2 \theta}{\partial z^2}\right)-K\phi \qquad (22)$$

with relevant boundary conditions:

$$y=0\ :\ u=0,\ \bar{v}=-(1+\varepsilon \operatorname{Cos}\pi z),\ w=0,\ \theta=1\ ,\ \phi=1 \qquad (23)$$

$$y\to\infty\ :\ u=U,\ \bar{v}=-1,\ \bar{w}=0,\ \theta=0\ ,\ \phi=0,\ p=p_\infty \qquad (24)$$

METHOD OF SOLUTION

We assume the solution of Equations 17 to 22 to be of the form:

$$u=u_0(y)+\varepsilon u_1(y,z)+0(\varepsilon^2) \qquad (25)$$

$$v=v_0(y)+\varepsilon v_1(y,z)+0(\varepsilon^2) \qquad (26)$$

$$w=w_0(y)+\varepsilon w_1(y,z)+0(\varepsilon^2) \qquad (27)$$

$$p=p_0(y)+\varepsilon p_1(y,z)+0(\varepsilon^2) \qquad (28)$$

$$\theta=\theta_0(y)+\varepsilon \theta_1(y,z)+0(\varepsilon^2) \qquad (29)$$

$$\phi=\phi_0(y)+\varepsilon \phi_1(y,z)+0(\varepsilon^2) \qquad (30)$$

with $p_0=p_\infty$, $w_0=0$ (31)

Substituting these in Equations 17 to 22 and equating the harmonic terms and neglecting ε^2 we get the following set of the differential equations:

Zeroth-order equations:

$$\frac{dv_0}{dy}=0 \qquad (32)$$

$$v_0\frac{du_0}{dy}=G_r\theta_0+G_m\phi_0+\frac{1}{R_e}\frac{d^2u_0}{dy^2}+MR_e(U-u) \qquad (33)$$

$$v_0\frac{d\theta_0}{dy}=\frac{1}{P_r R_e}\frac{d^2\theta_0}{dy^2}-Q\theta_0 \qquad (34)$$

$$v_0\frac{d\phi_0}{dy}=\frac{1}{S_c R_e}\frac{d^2\phi_0}{dy^2}+\frac{S_r}{R_e}\frac{d^2\theta_0}{dy^2}-K\phi_0 \qquad (35)$$

First-order equations:

$$\frac{\partial v_1}{\partial y}+\frac{\partial w_1}{\partial z}=0 \qquad (36)$$

$$-\frac{\partial u_1}{\partial y}+v_1\frac{du_0}{dy}=G_r\theta_1+G_m\phi_1+\frac{1}{R_e}\left(\frac{\partial^2 u_1}{\partial y^2}+\frac{\partial^2 u_1}{\partial z^2}\right)-MR_e u_1 \qquad (37)$$

$$-\frac{\partial v_1}{\partial y}=-\frac{1}{R_e^2}\frac{\partial p_1}{\partial y}+\frac{1}{R_e}\left(\frac{\partial^2 v_1}{\partial y^2}+\frac{\partial^2 v_1}{\partial z^2}\right) \qquad (38)$$

$$-\frac{\partial w_1}{\partial y}=-\frac{1}{R_e^2}\frac{\partial p_1}{\partial y}+\frac{1}{R_e}\left(\frac{\partial^2 w_1}{\partial y^2}+\frac{\partial^2 w_1}{\partial z^2}\right)-MR_e w_1 \qquad (39)$$

$$-\frac{\partial \theta_1}{\partial y}+v_1\frac{d\theta_0}{dy}=\frac{1}{P_r R_e}\left(\frac{\partial^2 \theta_1}{\partial y^2}+\frac{\partial^2 \theta_1}{\partial z^2}\right)-Q\theta_1 \qquad (40)$$

$$-\frac{\partial \phi_1}{\partial y}+v_1\frac{d\phi_0}{dy}=\frac{1}{S_c R_e}\left(\frac{\partial^2 \phi_1}{\partial y^2}+\frac{\partial^2 \phi_1}{\partial z^2}\right)+\frac{S_r}{R_e}\left(\frac{\partial^2 \theta_1}{\partial y^2}+\frac{\partial^2 \theta_1}{\partial z^2}\right)-K\phi_1 \qquad (41)$$

Subject to boundary conditions:

$$y=0\ :\ u_0=0,\ v_0=-1,\ \theta_0=1,\ \phi_0=1,\ u_1=0,\ v_1=-\operatorname{Cos}\pi z$$
$$w_1=0\ ,\ \theta_1=0\ ,\ \phi_1=0 \qquad (42)$$

$$y\to\infty\ :\ u_0=U\ ,\ v_0=-1,\ \theta_0=0\ ,\ \phi_0=0\ ,\ u_1=0\ ,\ v_1=0$$
$$,\ w_1=0\ ,\ p_1=0\ ,\ \theta_1=0\ ,\ \phi_1=0 \qquad (43)$$

The solution of Equations 32 to 35 under the boundary conditions 42 and 43 are

$$v_0=-1 \qquad (44)$$

$$\theta_0=e^{-ay} \qquad (45)$$

$$\phi_0=(1-a_1)e^{-by}+a_1e^{-ay} \qquad (46)$$

$$u_0=U+A_1e^{-ay}+A_2e^{-b_e y}+(-A_1-A_2-U)e^{-\lambda R_e y} \qquad (47)$$

where

$$a=\frac{P_rR_e+\sqrt{P_r^2R_e^2+4P_rR_eQ}}{2}\ ,\ a_1=\frac{-a^2S_rS_c}{a^2-S_cRa-KS_cR_e}\ ,\ \lambda=\frac{1+\sqrt{1+4M}}{2}\ ,$$

$$b=\frac{S_cR_e+\sqrt{S_c^2R_e^2+4KS_cR_e}}{2},$$

$$A_1=\frac{-G_ma_1R_e}{a^2-R_ea-MR_e^2}-\frac{G_rR_e}{a^2-R_ea-MR_e^2}\ ,\ A_2=\frac{-G_m(1-a_1)R_e}{b^2-R_eb-MR_e^2}$$

We shall first consider the Equations 36, 38 and 39 for $v_1(y, z)$, $w_1(y, z)$ and $p_1(y, z)$ which are independent of main flow component u_1, temperature field θ_1 and concentration field ϕ_1. The suction velocity $v_w = -(1+\varepsilon \operatorname{Cos} \pi z)$ consists of a uniform distribution -1 with superimposed weak sinusoidal distribution $\varepsilon \operatorname{Cos} \pi z$. Hence the velocity components v, w and p are also separated into mean and small sinusoidal components v_1, w_1 and p_1. We assume v_1, w_1 and p_1 to be of the following forms:

$$v_1 = -\pi v_{11}(y) \operatorname{Cos} \pi z \tag{48}$$

$$w_1 = v'_{11}(y) \operatorname{Sin} \pi z \tag{49}$$

$$p_1 = R_e^2\, p_{11}(y) \operatorname{Cos} \pi z \tag{50}$$

On substitution of Equations 48, 49 and 50, Equation 36 is satisfied and Equations 38 and 39 reduce to the following ordinary differential equations

$$v''_{11} + R_e v'_{11} - \pi^2 v_{11} = -\frac{R_e p'_{11}}{\pi} \tag{51}$$

$$v'''_{11} + R_e v''_{11} - \left(\pi^2 + M R^2\right) v'_{11} = -R_e \pi p_{11} \tag{52}$$

with relevant boundary conditions

$$y = 0 \quad : \quad v_{11} = \frac{1}{\pi} \quad , \quad v'_{11} = 0 \tag{53}$$

$$y \to \infty \; : \; v_{11} = 0 \; , \; v'_{11} = 0 \; , \; p_{11} = 0 \tag{54}$$

The solutions of these equations are:

$$v_{11} = \frac{1}{\pi\left(\bar{\xi} - \xi\right)}\left[\bar{\xi} e^{-\xi y} - \xi e^{-\bar{\xi} y}\right] \tag{55}$$

$$p_{11} = \frac{1}{R_e \pi^2\left(\bar{\xi} - \xi\right)}\left[\left(\pi^2 + M R_e^2 + R_e \bar{\xi} - \bar{\xi}^2\right) e^{-\bar{\xi} y} - \left(\pi^2 + M R_e^2 + R_e \xi - \xi^2\right) e^{-\xi y}\right]$$

$$= \frac{1}{R_e \pi^2\left(\bar{\xi} - \xi\right)}\left[\bar{\xi}_1 e^{-\bar{\xi} y} - \xi_1 e^{-\xi y}\right] \tag{56}$$

Where

$$\xi = \frac{R_e \lambda + \sqrt{R_e^2 \lambda^2 + 4\pi^2}}{2},$$

$$\bar{\xi} = \frac{R_e \bar{\lambda} + \sqrt{R_e^2 \bar{\lambda}^2 + 4\pi^2}}{2}, \quad \lambda = \frac{1 + \sqrt{1 + 4M}}{2},$$

$$\bar{\lambda} = \frac{1 - \sqrt{1 + 4M}}{2}, \quad \bar{\xi}_1 = \left(\pi^2 + M R_e^2 + R_e \bar{\xi} - \bar{\xi}^2\right),$$

$$\xi_1 = \left(\pi^2 + M R_e^2 + R_e \xi - \xi^2\right)$$

Hence the solutions for the velocity components v_1, w_1 and pressure p_1 are as follows:

$$v_1 = \frac{1}{\xi - \bar{\xi}}\left[\bar{\xi} e^{-\xi y} - \xi e^{-\bar{\xi} y}\right] \operatorname{Cos} \pi z \tag{57}$$

$$w_1 = \frac{\xi \bar{\xi}}{\pi\left(\xi - \bar{\xi}\right)}\left[e^{-\bar{\xi} y} - e^{-\xi y}\right] \operatorname{Sin} \pi z \tag{58}$$

$$p_1 = \frac{R_e \xi \bar{\xi}}{\pi^2\left(\bar{\xi} - \xi\right)}\left[\bar{\xi}_1 e^{-\bar{\xi} y} - \xi_1 e^{-\xi y}\right] \operatorname{Cos} \pi z \tag{59}$$

SOLUTION FOR FIRST ORDER FLOW, CONCENTRATION AND TEMPERATURE FIELD

We now consider Equations 30, 33 and 34. The solutions for velocity component u, temperature field θ and concentration field ϕ are also separated into mean and sinusoidal components u_1, θ_1 and ϕ_1. To reduce the partial differential Equations 30, 33, 34 into ordinary differential equations, we consider the following forms for u_1, θ_1 and ϕ_1.

$$u_1 = u_{11}(y) \operatorname{Cos} \pi z \tag{60}$$

$$\theta_1 = \theta_{11}(y) \operatorname{Cos} \pi z \tag{61}$$

$$\phi_1 = \phi_{11}(y) \operatorname{Cos} \pi z \tag{62}$$

Using the expressions for v_1, u_1, θ_1, ϕ_1 in Equations 37, 40 and 41 we get the following differential equations:

$$u''_{11} + R_e u'_{11} - \left(\pi^2 + M R_e^2\right) u_{11} = -\pi R_e v_{11} u'_0 - R_e G_r \theta_{11} - R_e G_m \phi_{11} \tag{63}$$

$$\theta''_{11} + P_r R_e \theta'_{11} - \left(\pi^2 + P_r R_e Q\right) \theta_{11} = -\pi P_r R_e v_{11} \theta'_0 \tag{64}$$

$$\phi''_{11} + S_c R_e \phi'_{11} - \left(\pi^2 + K\right) \phi_{11} = -\pi S_c R_e v_{11} \phi'_0 - S_c S_r \left(\theta''_{11} - \pi^2 \theta_{11}\right) \tag{65}$$

with the boundary conditions

$$\left.\begin{aligned} & y = 0 \; : \; u_{11} = 0, \; \theta_{11} = 0, \; \phi_{11} = 0 \\ & y \to \infty \; : u_{11} = 0, \; \theta_{11} = 0, \; \phi_{11} = 0 \end{aligned}\right\} \tag{66}$$

The solutions of Equations 64, 65 and 63 subject to boundary conditions (66) are

$$\theta_{11} = G_0 e^{-hy} + G_1 e^{-(\xi+a)y} + G_2 e^{-(\bar{\xi}+a)y} \quad (67)$$

$$\phi_{11} = H_0 e^{-my} + H_1 e^{-hy} + H_2 e^{-(\xi+a)y} + H_3 e^{-(\bar{\xi}+a)y} + H_4 e^{-(\xi+b_e)y} + H_5 e^{-(\bar{\xi}+b)y} \quad (68)$$

$$u_{11} = M_0 e^{-ny} + M_1 e^{-hy} + M_2 e^{-my} + M_3 e^{-(\xi+a)y} + M_4 e^{-(\bar{\xi}+a)y} + M_5 e^{-(\xi+b)y} + +M_6 e^{-(\bar{\xi}+b)y} + M_7 e^{-(\xi+\lambda R_e)y} + M_8 e^{-(\bar{\xi}+\lambda R_e)y} \quad (69)$$

where

$$G_1 = \frac{aP_rR_e\bar{\xi}}{(\bar{\xi}-\xi)\left\{(\xi+a)^2 - P_rR_e(\xi+a) - (\pi^2 + P_rR_eQ)\right\}},$$

$$G_2 = \frac{-aP_rR_e\xi}{(\bar{\xi}-\xi)\left\{(\bar{\xi}+a)^2 - P_rR_e(\bar{\xi}+a) - (\pi^2 + P_rR_eQ)\right\}}, \; G_0 = -(G_1+G_2),$$

$$h = \frac{P_rR_e + \sqrt{P_r^2R_e^2 + 4(\pi^2 + P_rR_eQ)}}{2},$$

$$m = \frac{S_cR_e + \sqrt{S_c^2R_e^2 + 4(\pi^2 + K)}}{2},$$

$$E_1 = -S_cS_rG_0(h^2-\pi^2), \; E_2 = -S_cS_rG_1\left\{(\xi+a)^2-\pi^2\right\}, \; E_3 = -S_cS_rG_2\left\{(\bar{\xi}+a)^2-\pi^2\right\},$$

$$B_1 = \frac{(1-a_1)bS_cR_e\xi}{(\bar{\xi}-\xi)}, \; B_2 = \frac{a\,a_1S_cR_e\bar{\xi}}{(\bar{\xi}-\xi)}, \; B_3 = \frac{-S_cR_eb\xi(1-a_1)}{(\bar{\xi}-\xi)}, \; B_4 = \frac{-a\,a_1S_cR_e\xi}{(\bar{\xi}-\xi)},$$

$$H_1 = \frac{E_1}{h^2 - S_cR_e h - (\pi^2+K)}, \; H_2 = \frac{B_2+E_2}{(\xi+a)^2 - S_cR_e(\xi+a) - (\pi^2+K)},$$

$$H_3 = \frac{B_4+E_3}{(\bar{\xi}+a)^2 - S_cR_e(\bar{\xi}+a) - (\pi^2+K)}, \; H_4 = \frac{B_1}{(\xi+b)^2 - S_cR_e(\xi+b) - (\pi^2+K)},$$

$$H_5 = \frac{B_3}{(\bar{\xi}+b)^2 - S_cR_e(\bar{\xi}+b) - (\pi^2+K)}, \; H_0 = -\sum_{i=1}^{5} H_i$$

$$, \; n = \frac{R_e + \sqrt{R_e^2 + 4(\pi^2 + MR_e^2)}}{2},$$

$$K_1 = \frac{a\,A_1R_e\bar{\xi}}{(\xi-\bar{\xi})},$$

$$K_2 = \frac{A_2bR_e\bar{\xi}}{(\bar{\xi}-\xi)}, \; K_3 = -\frac{\bar{\xi}\lambda R_e^2(A_1+A_2+U)}{(\bar{\xi}-\xi)}, \; K_4 = \frac{-a\,A_1R_e\xi}{(\bar{\xi}-\xi)},$$

$$K_5 = -\frac{A_2bR_e\xi}{(\bar{\xi}-\xi)}, \; K_6 = \lambda R_e^2(A_1+A_2+U)\xi,$$

$$L_1 = R_e(G_rG_0 + G_mH_1), \; L_2 = -G_mH_0R_e$$

$$L_3 = K_1 - G_rG_1R_e - G_mH_2R_e, \; L_4 = K_4 - G_mH_3R_e - R_eG_rG_2, \; L_5 = K_2 - G_mH_4R_e$$

$$L_6 = K_5 - G_mH_5R_e, \; M_1 = \frac{L_1}{h^2 - R_eh - (\pi^2 + MR_e^2)}, \; M_2 = \frac{L_2}{m^2 - R_em - (\pi^2 + MR_e^2)},$$

$$M_3 = \frac{L_3}{(\xi+a)^2 - R_e(\xi+a) - (\pi^2 + MR_e^2)}, \; M_4 = \frac{L_4}{(\bar{\xi}+a)^2 - R_e(\bar{\xi}+a) - (\pi^2 + MR_e^2)},$$

$$M_5 = \frac{L_5}{(\xi+b)^2 - R_e(\xi+b) - (\pi^2 + MR_e^2)}, \; M_6 = \frac{L_6}{(\bar{\xi}+b)^2 - R_e(\bar{\xi}+b) - (\pi^2 + MR_e^2)},$$

$$M_7 = \frac{K_3}{(\xi+\lambda R_e)^2 - R_e(\xi+\lambda R_e) - (\pi^2 + MR_e^2)},$$

$$M_8 = \frac{K_6}{(\bar{\xi}+\lambda R_e)^2 - R_e(\bar{\xi}+\lambda R_e) - (\pi^2 + MR_e^2)},$$

$$M_0 = -\sum_{i=1}^{8} M_i$$

Skin friction at the plate

The non-dimensional skin-friction at the plate in direction of the free steam is given by

$$\tau = \frac{\mu \left.\frac{\partial \bar{u}}{\partial \bar{y}}\right)_{\bar{y}=0}}{\rho V_0^2} = -\frac{1}{R_e}\left[u_0'(0) + \varepsilon u_{11}'(0)\cos\pi z\right] = \tau_0 + \varepsilon Q_1 \cos\pi z \quad (70)$$

where

$$\tau_0 = -\frac{1}{R_e}u_0'(0) = \frac{aA_1}{R_e} + \frac{bA_2}{R_e} - \lambda(A_1 + A_2 + U) \quad (71)$$

and

$$Q_1 = -\frac{1}{R_e}u_{11}'(0)$$
$$= \frac{1}{R_e}\left[\begin{matrix} nM_0 + hM_1 + mM_2 + (\xi+a)M_3 + (\bar{\xi}+a)M_4 + (\xi+b)M_5 \\ +(\bar{\xi}+b)M_6 + (\lambda R_e + \xi)M_7 + (\lambda R_e + \bar{\xi})M_8 \end{matrix}\right] \quad (72)$$

The co-efficient of rate of heat transfer

The heat flux from the plate to the in terms of Nusselt number Nu is given by

$$Nu = -\frac{k}{\rho V_0 C_p(\bar{T}_w - \bar{T}_\infty)}\left(\frac{\partial \bar{T}}{\partial \bar{y}}\right)_{y=0} = -\frac{1}{P_rR_e}\left.\frac{\partial\theta}{\partial y}\right]_{y=0} = Nu_0 + \varepsilon Q_2 \cos\pi z \quad (73)$$

Where

$$Nu_0 = -\frac{\theta_0'(0)}{P_r R_e} = \frac{a}{P_r R_e} \tag{74}$$

And

$$Q_2 = -\frac{\theta_{11}'(0)}{P_r R_e} = \frac{1}{P_r R_e}\left[hG_0 + (\xi + a)G_1 + (\bar{\xi} + a)G_2\right] \tag{75}$$

The coefficient of mass transfer

The mass flux at the wall y = 0 in terms of Sherwood number Sh is given by

$$Sh = \frac{-D_M}{V_0(\bar{C}_w - \bar{C}_\infty)}\left(\frac{\partial \bar{C}}{\partial \bar{y}}\right)_{y=0} = -\frac{1}{S_c R_e}\frac{\partial \phi}{\partial y}\bigg]_{y=0} = -\frac{1}{S_c R_e}\left[\phi_0'(0) + \varepsilon \phi_{11}' \mathrm{Cos}\pi z\right]$$

$$= Sh_0 + \varepsilon Q_3 \mathrm{Cos}\,\pi z \tag{76}$$

Where

$$Sh_0 = -\frac{1}{S_c R_e}\left[b(1 - a_1) + a a_1\right] \tag{77}$$

and

$$Q_3 = -\frac{1}{S_c R_e}\phi_{11}'(0) = \frac{1}{S_c R_e}\begin{bmatrix} mH_0 + hH_1 + (\xi + a)H_2 + (\bar{\xi} + a)H_3 \\ (\xi + b)H_4 + (\bar{\xi} + b)H_5 \end{bmatrix} \tag{78}$$

Current density

The current density $\vec{J}$ is given by

$$\vec{J} = \sigma \vec{q} \times \vec{B} = \sigma B_0\left(-\hat{i}\,\bar{w} + \hat{k}\,\bar{u}\right) \tag{79}$$

The magnitude of $\vec{J}$ is given

by $\left|\vec{J}\right| = \sigma B_0 \sqrt{\bar{w}^2 + \bar{u}^2} = \sigma B_0 V_0 \sqrt{u^2 + w^2}$ (80)

The current density (in magnitude) in non dimensional form is given by:

$$J_c = \frac{\left|\vec{J}\right|}{\sigma B_0 V_0} = \sqrt{u^2 + w^2} = u\sqrt{1 + \left(\frac{w}{u}\right)^2} = u$$

(since $\frac{w}{u} << 1$) (81)

That is, the magnitude of the non dimensional current density is proportional to the boundary layer velocity.

RESULTS AND DISCUSSION

In order to study the effects of heat sink parameter (Q), Reynolds number (R_e), and chemical reaction parameter (K), we have carried out the data tabulations for u, θ_0, ϕ_0, Q_1, Q_2, Q_3 and τ_0 which are respectively the dimensional velocity, zeroth order temperature, zeroth order species concentration, amplitudes of the first order skin friction, Nusselt number and Sherwood number; the zeroth order skin friction at the plate y = 0 and their values are demonstrated in the graphs. Throughout our discussion P_r (Prandtl number) is considered to be equal to 71 which corresponds to air. Since the water vapor is used as a diffusing chemical species of common interest in air therefore the values of S_c is taken to be 0.60 (water vapor). The values of the Grashof number G_r for heat transfer has been chosen as 10 (externally cooled plate) whereas the values of Grashof number G_m for mass transfer is considered to be 15, the free steam velocity is selected to be 1 and the small reference parameter ε is chosen as 0.001 and the remaining parameters namely chemical reaction parameter (K), heat sink parameter (Q), Reynolds number (R_e), Soret number S_r are chosen arbitrarily.

Figures 1, 2 and 3 exhibit the variation of velocity profile u against y for different values of chemical reaction parameter (K), heat sink parameter (Q) and Hartmann number (M). It is seen from these figures that the velocity quickly increases up to some thin layer of the liquid adjacent to the plate and after this, fluid velocity decreases asymptotically towards 1 as $y \to \infty$; that is, in the free steam. This shows that the buoyancy effects (due to concentration and temperature differences) are significant near the hot plate.

It is observed from Figure 1 that the fluid motion is retarded (that is, the fluid velocity decreases) on account of chemical reaction. This shows that the consumption of chemical species leads to fall in the concentration field which in turn diminishes the buoyancy effects due to concentration gradients. Consequently, the flow field is decelerated. It is also inferred from Figures 2 and 3 that the heat sink parameter (Q) as well as Hartmann number (M) impedes the fluid motion. In other words, fluid motion is retarded due to application of transverse magnetic field. This phenomenon clearly agrees with the fact that Lorentz force that appears due to interaction of the magnetic field and fluid velocity resists the fluid motion.

Figure 4 demonstrates the variation of zeroth order fluid temperature θ_0 against y under the effect of heat sink parameter (Q). It is clear from this figure that zeroth order fluid temperature θ_0 asymptotically falls from 1 to zero as $y \to \infty$. The same figure further indicates that the heat sink parameter results in a steady decrease in the zeroth order fluid temperature.

The variation of zeroth order species concentration ϕ_0 versus y under the influences of heat sink parameter (Q) and chemical reaction parameter (K) have been presented in Figures 5 and 6. These figures show that

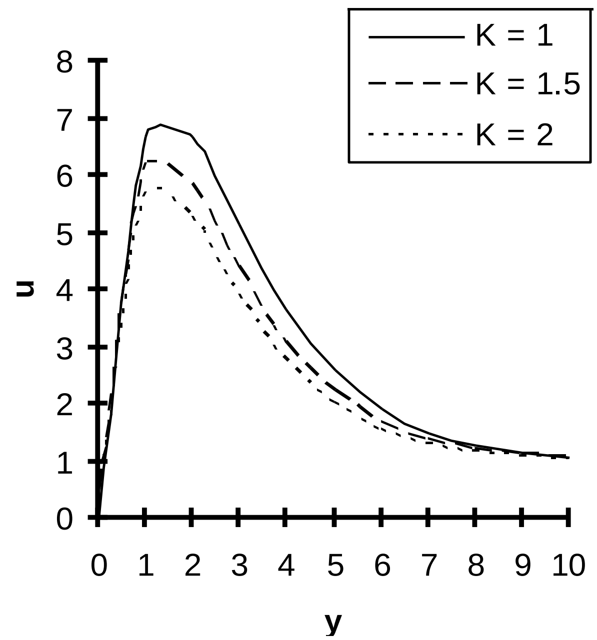

Figure 1. Velocity distribution versus y for K when Q =1, M = 1, R_e = 0.5, S_r = 0.5.

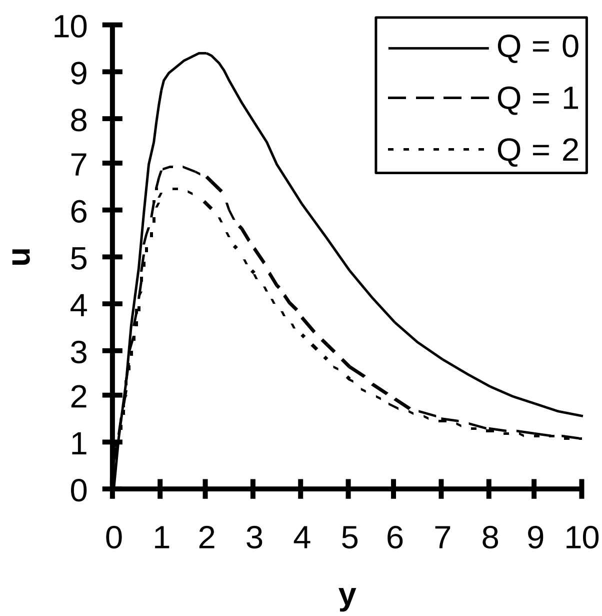

Figure 2. Velocity distribution versus y for Q when K =1, M = 1, R_e = 0.5, S_r = 0.5.

zeroth order concentration of the fluid fall under the effect of heat sink parameter (Q) and chemical reaction parameter (K). Moreover, it is noticed from these figure that ϕ_o asymptotically decreases from maximum value $\phi_o = 1$ to its minimum value $\phi_o = 0$ as one moves far away the plate ($y \to \infty$).

Figures 7, 8 and 9 depict the variation of amplitude of the perturbed part of skin-friction Q_1 versus Reynolds number R_e. From these figures we observe that magnetic field effect as well as heat sink effect causes Q_1 to decrease whereas Q_1 increases for the increasing values of chemical reaction parameter. There is an

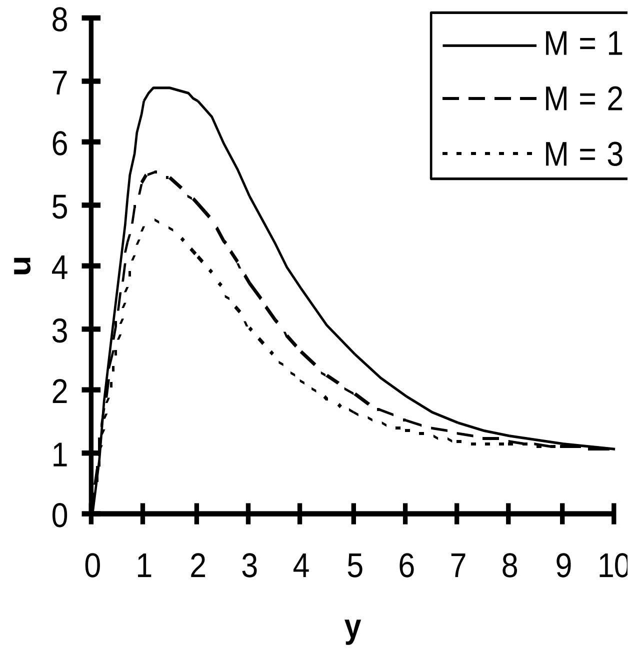

Figure 3. Velocity distribution versus y for M when Q =1, K = 1, R_e =0 .5, S_r = 0.5.

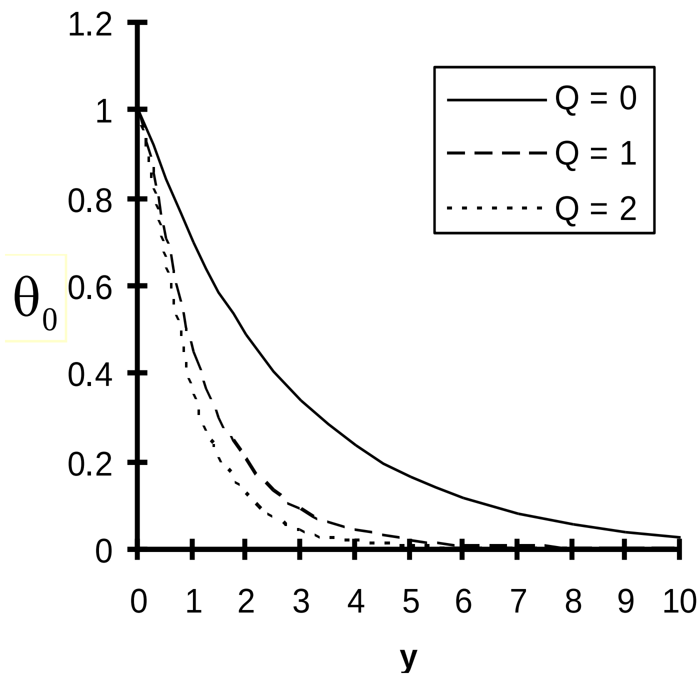

Figure 4. Zeroth order temperature distribution versus y for Q when R_e = 0.5.

indication from these figures that Q_1 falls as R_e increases. That is for low viscosity Q_1 is not significantly affected by heat sink parameter (Q), chemical reaction parameter (K) or by Hartmann number (M).

The influence of heat sink parameter (Q) on the amplitude of Q_2 of the perturbed part of the Nusselt number is displayed in Figure 10. It is noticed from the figure that an increase in the value of Reynolds number

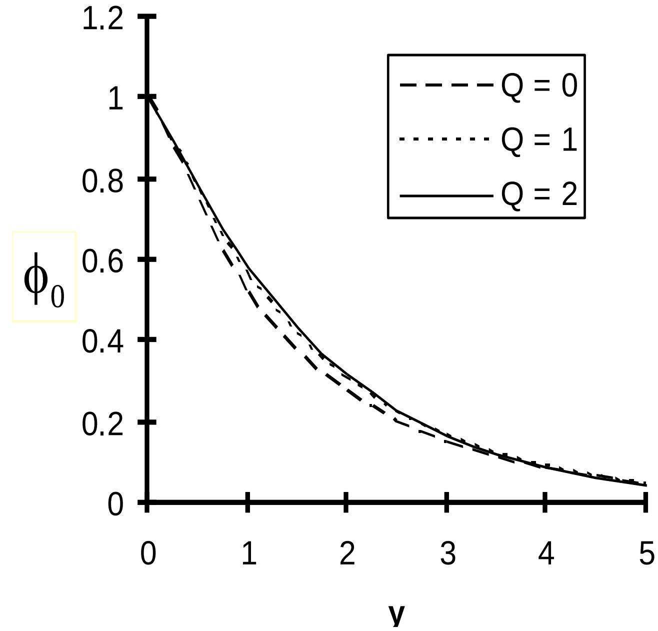

Figure 5. Zeroth order concentration profile versus y for Q when K = 1, R_e = 0.5, S_r = 0.5.

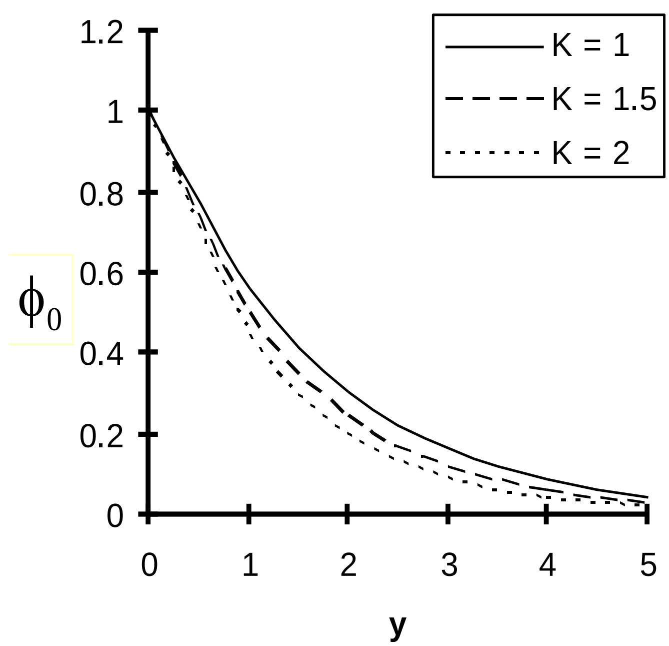

Figure 6. Zeroth order concentration profile versus y for K when Q = 1, R_e = 0.5, S_r = 0.5.

(R_e) or heat sink parameter (Q) causes Q_2 to increase; that is, Q_2 drops due to high viscosity or low strength of heat sink.

Figures 11 and 12 exhibits the change in behaviour of amplitude, of perturbed part, and of the Sherwood number Q_3 under the influence of the Reynolds number R_e, the chemical reaction parameter (K) and

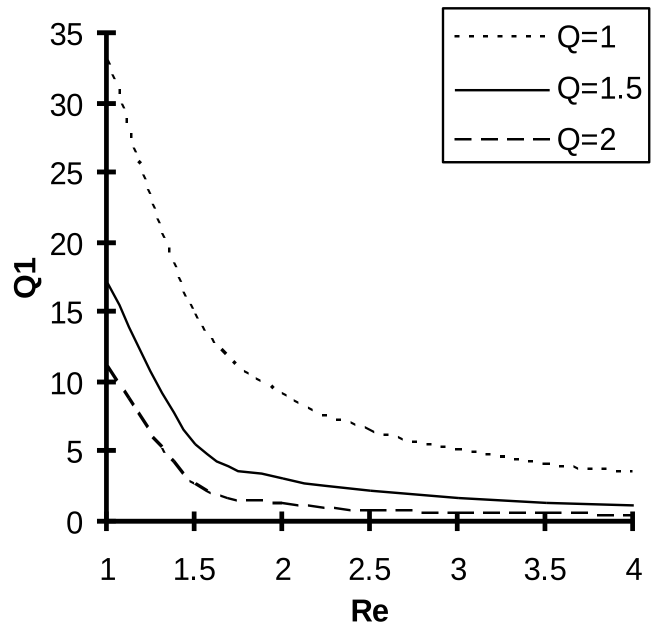

Figure 7. The amplitude Q_1 of the first order skin friction versus R_e for K=1, M=1, S_r=0.5.

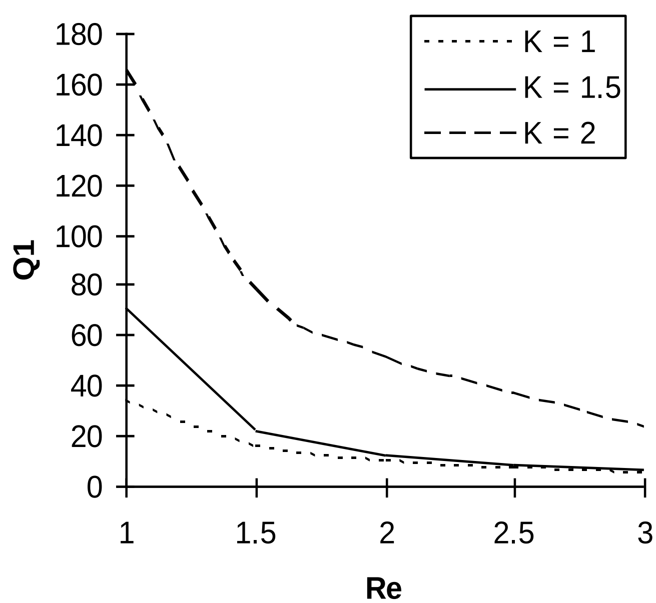

Figure 8. The amplitude Q_1 of the first order skin friction versus R_e for Q=1, M=1, S_r= 0.5.

heat sink parameter (Q). These figures show that Q_3 is increased due to chemical reaction effect where as there is a steady decline in Q_3 when heat sink parameter (Q) is increased.

The variation of the zeroth order skin friction τ_0 at the plate y = 0 under the influence of chemical reaction parameter (K), heat sink parameter (Q) and Hartmann

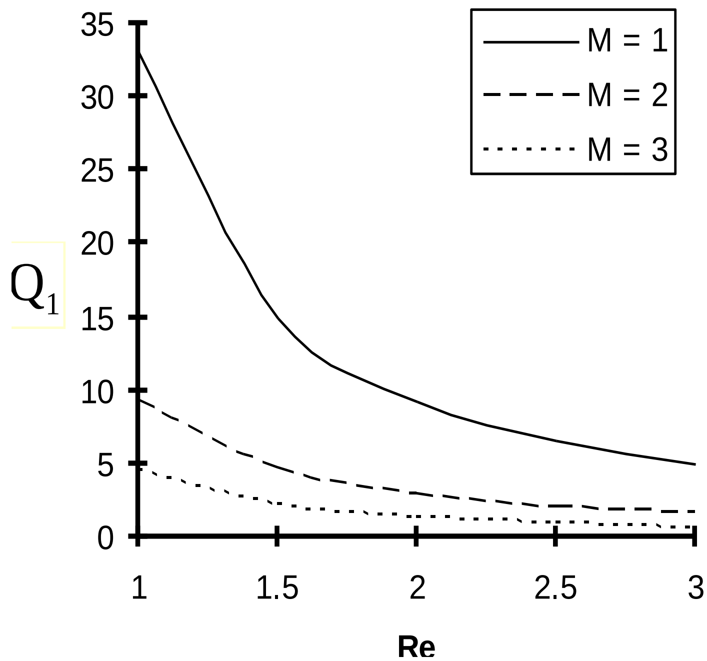

Figure 9. The amplitude Q_1 of the first order skin friction versus R_e for K = 1, Q = 1, S_r = 0.5.

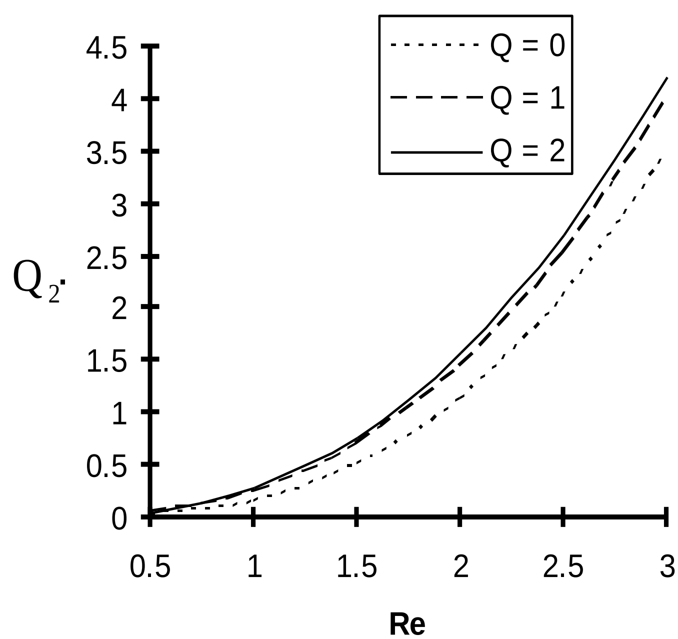

Figure 10. The amplitude Q_2 of the first order Nusselt number versus R_e for K = 1, S_r = 0.5.

number (M) are presented respectively in Figures 13, 14 and 15. It is noticed from these figures that the magnitude of viscous drag at the plate decreases due to the chemical reaction parameter (K), heat sink (Q) and

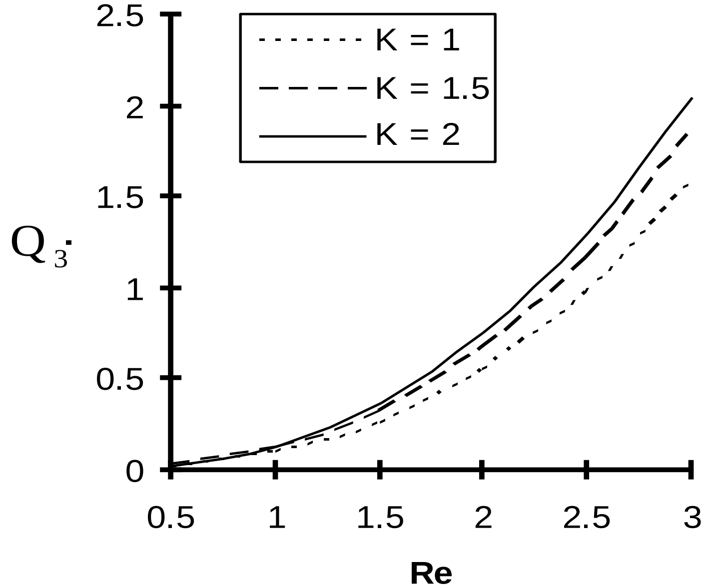

Figure 11. The amplitude Q_3 of the first order Sherwood number versus R_e for Q=1, S_r=0.5.

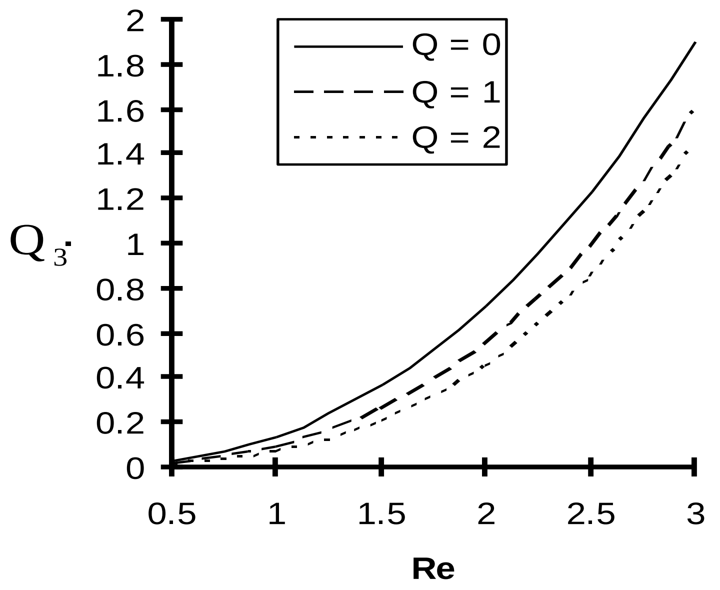

Figure 12. The amplitude Q_3 of the first order Sherwood number versus R_e for Q =1, S_r=0.5.

magnetic field (M).

Conclusion

1. The chemical reaction, heat sink and magnetic field lead the fluid motion to retard. Thus the chemically reacting fluid motion may be controlled with the application of heat sink and magnetic field.
2. The heat sink results in a steady decrease in the fluid temperature. Hence the fluid temperature may be controlled by using a suitable heat sink.

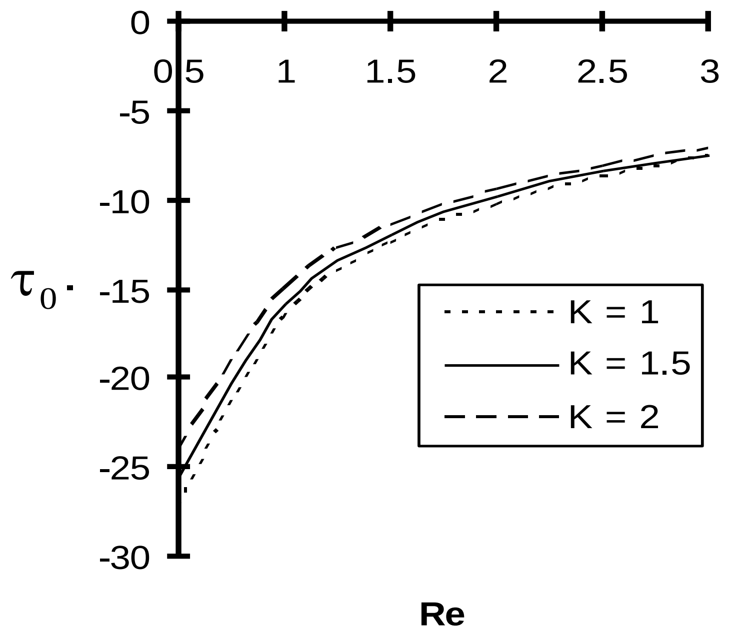

Figure 13. The zeroth order skin friction τ_0 at the plate versus R_e for Q = 1, M=1, S_r=0.5.

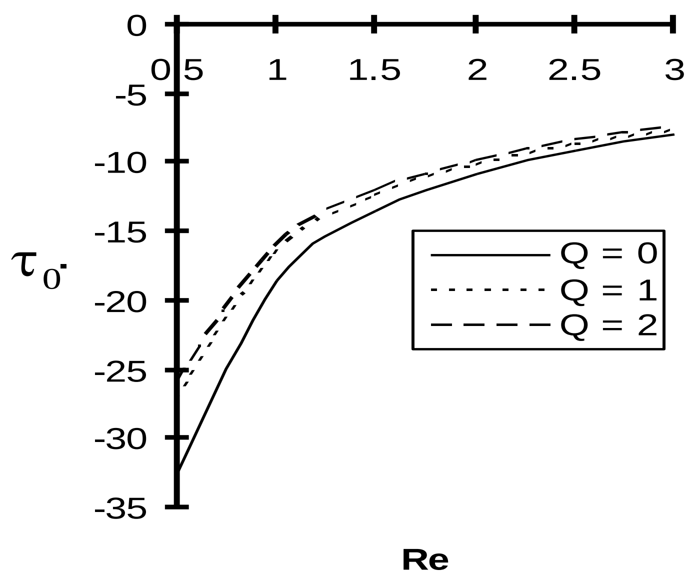

Figure 14. The zeroth order skin friction τ_0 at the plate versus R_e for Q = 1, M=1, S_r=0.5.

3. The concentration of the fluid rises under the effect of heat sink whereas it falls due to the effect of chemical reaction.
4. Magnitude of the first order skin friction increases due to chemical reaction effect and it decreases under the effects of absorption heat sink and the applied transverse magnetic field.
5. The first order Nusselt number drops due to high viscosity or low strength heat sink.
6. The heat absorbing sink leads the first order Sherwood

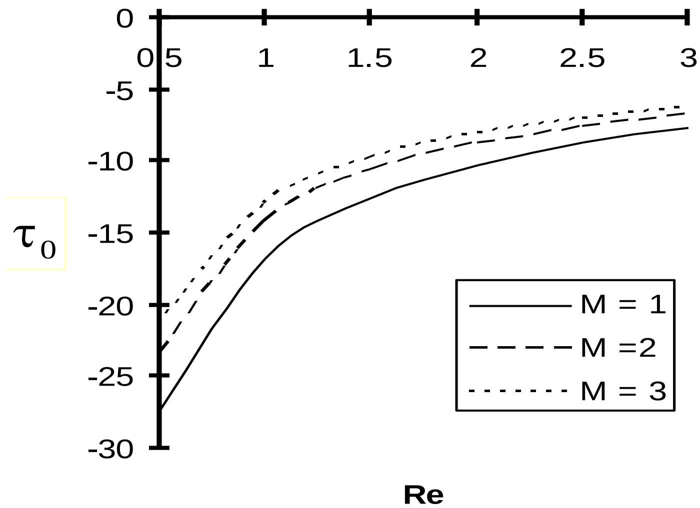

Figure 15. The zeroth order skin friction τ_0 at the plate versus R_e for Q = 1, K=1, S_r=0.5.

number to fall but it rises under the effect of chemical reaction parameter.

7. Magnitude of the zeroth order skin friction diminishes due to chemical reaction effect, magnetic field as well as the heat sink.

Nomenclature: $\vec{B}$, magnetic induction vector; B_0, strength of applied magnetic field; $\bar{C}_\infty$, species concentration in the free stream; $\bar{C}_w$, species concentration at the plate; $\bar{C}_p$, specific heat at constant pressure; D_M, chemical molecular diffusivity; D_T, chemical thermal diffusivity; $\vec{E}$, electric field; $\vec{g}$, gravitational acceleration; **g,** acceleration due to gravity; G_r, Grashof number for heat transfer; G_m, Grashof number for mass transfer; $\vec{J}$, electric current density; **k,** thermal conductivity; $\bar{K}$, first order chemical reaction; **K,** chemical reaction parameter; **L,** wave length of the periodic suction; **M,** Hartmann number; $\bar{p}$, pressure; $\bar{p}_\infty$, pressure in the free steam; **p,** non dimensional pressure; p_∞, non dimensional pressure in the free steam; $\vec{q}$, velocity vector; $\bar{Q}$, first order heat sink; **Q,** non dimensional first order heat sink; R_e, Reynolds number; S_r, Soret number; P_r, Prandtl number; S_c, Schmidt number; $\bar{T}$, temperature in the boundary layer; $\bar{T}_w$, temperature at the plate; $\bar{T}_\infty$, fluid temperature at the free steam; $\bar{U}$, free steam velocity; U, non dimensional free steam velocity; $(\bar{u},\bar{v},\bar{w})$, components of the fluid velocity; (u,v,w), non dimensional components of the fluid velocity; V_0, mean suction velocity; $(\bar{x},\bar{y},\bar{z})$, coordinate system; $\hat{i},\hat{j},\hat{k}$, unit vectors in the increasing direction of $\bar{x},\bar{y},\bar{z}$; $\vec{J}\times\vec{B}$, Lorentz force per unit volume; α, thermal diffusivity; β, coefficient of volume expansion for heat transfer; $\bar{\beta}$, coefficient of volume expansion for mass transfer; σ, electrical conductivity; ν, kinematic viscosity; ρ, density of the fluid; ε, small reference parameter; θ, non dimensional temperature; ϕ, non dimensional concentration; φ, viscous dissipation of energy per unit volume; μ, coefficient of viscosity.

REFERENCES

Ahmed N, Sarma D, Sarma D (2005). MHD free and force convective flow and mass transfer through a porous medium. Far East J. Appl. Math. 21(3):271.

Ahmed N, Sarma D (1997). Three dimensional free convective flow and heat transfer through a porous medium, Indian J. Pure Appl. Math. 26(10):1345.

Ahmed N, Sarma HK (2010). Effect on thermal diffusion on a three-dimensional MHD mixed convection with mass transfer flow past a porous vertical plate, J. energy, Heat Mass Transfer 32:199-221.

Ahmed N, Kalita H (2010). Oscillatory MHD free convective flow through a porous medium with mass transfer, Soret effect and chemical

reaction, Indian J. Sci. Technol. 3(8):919-924.
Ahmed N, Sarma D, Barua DP (2006). Three-dimensional free convective flow and mass transfer along a porous vertical plate, Bulletin of the Allahabad Mathematical Society. 21:125-141.
Bejan A, Khair KR (1985). Heat and mass transfer in a porous medium, Int. J. Heat Transfer**.** 28:902-918.
Choudhury RC, Chand T (2002). Three-Dimensional Flow and Heat Transfer through Porous Medium. Int. J. Appl. Mech. Eng. 7(4):1141-1156.
Cramer KR, Pai SI (1973). Magneto Fluid Dynamics for Engineers and Applied physicists, McGraw Hill Book Company, New York.
Devi SPA, Kandasamy R (2000). Effect of chemical reaction, heat transfer and mass transfer on MHD flow past a semi-infinite plate, Z. Angew. Math. Mech. 80:697-701.
Epstein IR, Pojman JA (1998). An introduction to non linear chemical dynamics, Oxford University Press, Oxford.
Ferraro VCA, Plumpton C (1966). An introduction to magneto fluid mechanics, Clarandon Press, Oxford.
Gray P, Scott SK (1990). Chemical oscillation and instabilities: Nonlinear chemical kinetics, Oxford University Press, Oxford.
Jain NC, Gupta P (2006). Three-Dimensional Free Convection Couetee Flow with Transpiration Cooling, J. Zhejiang University Sci. A. 7(3):340-346.
Raptis A, Kafousias N (1982). Magneto hydrodynamic free convective flow and mass transfer through a porous medium bounded by an infinite vertical porous plate with constant heat flux. Can. J. Phys. 60:1724-1729.
Sanyal DC, Bhattacharya S (1992). Similarity solutions of an unsteady incompressible thermal MHD boundary layer flow by group theoretic approach, Indian J. Eng. Sci. 30:561-569.

academicJournals

Related Journals Published by Academic Journals

- African Journal of Mathematics and Computer Science Research
- African Journal of Pure and Applied Chemistry
- Journal of Geology and Mining Research
- Journal of Environmental Chemistry and Ecotoxicology
- Journal of Internet and Information Systems
- Journal of Oceanography and Marine Science
- Journal of Petroleum Technology and Alternative Fuels